

Synthesis of epitaxial TaO₂ thin films on Al₂O₃ by suboxide molecular-beam epitaxy and thermal laser epitaxy

Yorick A. Birkhölzer,^{1, a)} Anna S. Park,^{1, 2, a)} Noah Schnitzer,^{1, 3} Jeffrey Z. Kaaret,⁴ Benjamin Z. Gregory,¹ Tomas A. Kraay,¹ Tobias Schwaigert,^{1, 2} Matthew R. Barone,^{1, 2} Brendan D. Faeth,² Felix V.E. Hensling,⁵ Iris C.G. van den Bosch,⁶ Ellen M. Kiens,⁶ Christoph Baeumer,⁶ Enrico Bergamasco,⁷ Markus Grüninger,⁷ Alexander Bordovalos,^{8, 9} Suresh Chaulagain,^{8, 9} Nikolas J. Podraza,^{8, 9} Waldemar Tokarz,¹⁰ Wojciech Tabis,¹⁰ Matthew J. Wahila,¹¹ Suchismita Sarker,¹² Christopher J. Pollock,¹² Shun-Li Shang,¹³ Zi-Kui Liu,¹³ Nongnuch Artrith,¹⁴ Frank M.F. de Groot,¹⁴ Nicole A. Benedek,¹ Andrej Singer,¹ David A. Muller,^{2, 3, 4} and Darrell G. Schlom^{1, 2, 3, 15}

¹⁾Department of Materials Science and Engineering, Cornell University, Ithaca, New York 14853, USA

²⁾Platform for the Accelerated Realization, Analysis, and Discovery of Interface Materials (PARADIM), Cornell University, Ithaca, New York 14853, USA

³⁾Kavli Institute at Cornell for Nanoscale Science, Ithaca, New York 14853, USA

⁴⁾School of Applied and Engineering Physics, Cornell University, Ithaca, New York 14853, USA

⁵⁾Max Planck Institute for Solid State Research, 70569 Stuttgart, Germany

⁶⁾MESA+ Institute for Nanotechnology, University of Twente, 7500 AE, Enschede, The Netherlands

⁷⁾Institute of Physics II, University of Cologne, 50937 Cologne, Germany

⁸⁾Department of Physics and Astronomy, University of Toledo, Toledo, Ohio 43606, USA

⁹⁾Wright Center for Photovoltaics Innovation and Commercialization, University of Toledo, Toledo, Ohio 43606, USA

¹⁰⁾Faculty of Physics and Applied Computer Science, AGH University of Krakow, 30-059, Krakow, Poland

¹¹⁾Analytical and Diagnostics Lab, Binghamton University, State University of New York, Binghamton, New York 13902, USA

¹²⁾Cornell High Energy Synchrotron Source, Wilson Laboratory, Cornell University, Ithaca, New York 14853, USA

¹³⁾Department of Materials Science and Engineering, The Pennsylvania State University, University Park, Pennsylvania 16802, USA

¹⁴⁾Debye Institute for Nanomaterials Science, Utrecht University, 3584 CG, Utrecht, The Netherlands

¹⁵⁾Leibniz-Institut für Kristallzüchtung, Max-Born-Str. 2, 12489 Berlin, Germany

(*Electronic mail: schlom@cornell.edu)

(*Electronic mail: y.birkholzer@cornell.edu)

(Dated: 9 January 2026)

Tantalum dioxide (TaO₂) is a metastable tantalum compound. Here, we report the epitaxial stabilization of TaO₂ on Al₂O₃ (1̄102) (*r*-plane sapphire) substrates using suboxide molecular-beam epitaxy (MBE) and thermal laser epitaxy (TLE), demonstrating single-oriented, monodomain growth of anisotropically strained thin films. Microstructural investigation is performed using synchrotron X-ray diffraction and scanning transmission electron microscopy. The tetravalent oxidation state of tantalum is confirmed using X-ray absorption and photoemission spectroscopy as well as electron energy-loss spectroscopy. Optical properties are investigated via spectroscopic ellipsometry and reveal a 0.3 eV Mott gap of the tantalum 5d electrons. Density-functional theory and group theoretical arguments are used to evaluate the limited stability of the rutile phase and reveal the potential to unlock a hidden metal-insulator transition concomitant with a structural phase transition to a distorted rutile phase, akin to NbO₂. Our work expands the understanding of tantalum oxides and paves the way for their integration into next-generation electronic and photonic devices.

I. INTRODUCTION

New materials with tunable electrical and optical conductivities can be a tremendous boon to the development of next-generation fast and energy-efficient nanoelectronics. Such materials may exhibit substantial changes between high-conductivity (“on”) and low-conductivity (“off”) states in response to thermodynamic control parameters, such as strain

or temperature. Unfortunately, most existing materials are either metallic or insulating, with limited ability to modify their conductivity. Historically, advancements in microelectronics have relied on tuning semiconductor conductivity through chemical doping and the electric-field effect. Materials undergoing a thermodynamic phase transition offer an exciting alternative to conventional semiconductors, enabling potential breakthroughs in device design. Among these, materials exhibiting a metal-insulator transition (MIT) are particularly intriguing.¹ Yet, such materials are rare, and even fewer exhibit an MIT above room temperature, limiting their integration.

^{a)}contributed equally

tion in practical devices.² Expanding the library of MIT materials is therefore essential to broadening their applications.

The archetypical compound exhibiting an MIT is VO₂, with a transition temperature of 65 °C. Shortly after the discovery of the MIT in 3d¹ VO₂,³ a similar effect was discovered in 4d¹ NbO₂ albeit at a much higher temperature of 807 °C.^{4,5} Thus far, high-quality samples of the 5d¹ analog TaO₂ have remained elusive. The d¹ oxides VO₂, NbO₂, and TaO₂ crystallize in the rutile structure (space group *P4₂/mnm*, # 136) at high temperature. Interest in TaO₂ is also motivated by the desire to compare it with its isoelectronic sulfide analog, TaS₂, which exhibits greater thermodynamic stability. Unlike the oxide, TaS₂ crystallizes in layered polymorphs, referred to as 1T (trigonal), 2H (hexagonal), and 3R (rhombohedral), similar to MoS₂. TaS₂ is renowned for its exotic electronic properties including an MIT, charge-density wave,⁶ and superconductivity.^{7–9} Furthermore, the conductivity can be tuned dynamically by electrical pulses^{10,11} as well as by ultrashort light pulses.¹²

Beyond its immediate relevance to MIT materials, studying TaO₂ could inform advancements in quantum information processing. Tantalum is a key material in the fabrication of superconducting quantum bits,^{13–15} and understanding its oxides may help mitigate decoherence from surface defects caused by uncontrolled oxidation.^{16,17} Furthermore, tantalum monoxide (TaO) has been identified as a superconductor with a critical temperature surpassing that of tantalum metal,^{18,19} further underscoring the need to explore tantalum oxides comprehensively. Last but not least, sub-stoichiometric tantalum oxides (Ta₂O_{5-x}, TaO_{2-x}) are technologically relevant to resistive switching memories. The resistive switching phenomenon in these devices is attributed to the reversible formation and rupture of conductive filaments within the tantalum oxide layer, typically associated with the movement of oxygen vacancies.²⁰

The inherent tendency of tantalum oxides to form oxygen vacancies and exhibit multiple valence states presents significant challenges in stabilizing intermediate oxidation states, particularly Ta⁴⁺ in TaO₂. Reports of the synthesis of bulk TaO₂ are scarce. Historically, some researchers focused on the partial reduction of Ta₂O₅,²¹ while others attempted the oxidation of TaC²² or experimented with redox reactions of tantalum with a different metal oxide.²³ None of these approaches resulted in the realization of phase-pure TaO₂. Syono *et al.*²⁴ used shock reduction at \approx 60 GPa to dissociate Ta₂O₅ under high pressure and high temperature and obtained a specimen with the rutile structure – albeit not phase-pure either (maximum yield \approx 70 %). Subsequent annealing of the material in an oxygen atmosphere resulted in a rutile structure with reduced lattice parameters, which the authors referred to as Ta_{0.8}O₂.

We are only aware of one report of the growth of epitaxial TaO₂ thin films. Muraoka *et al.*²⁵ utilized pulsed-laser deposition and employed a buffer layer of NbO₂ to epitaxially stabilize TaO₂ on Al₂O₃ (0001) (*c*-plane sapphire), achieving an orientation relationship of TaO₂ (100) on NbO₂ (110) on Al₂O₃ (0001). Their attempts to grow TaO₂ directly on

c-plane sapphire were unsuccessful.

In this work, we demonstrate the buffer-free epitaxial growth of anisotropically strained TaO₂ on *r*-plane sapphire (Al₂O₃ (1102)) using suboxide molecular-beam epitaxy (*S*-MBE) and thermal laser epitaxy (TLE).

The remainder of this article is organized as follows. Section II outlines the synthesis of TaO₂ thin films and the experimental techniques employed for their characterization. The experimental results and their discussion are presented in Section III. Section IV provides a summary of the first-principles calculations, which are described in detail in the supplementary material. Finally, Section V presents the conclusions and outlook.

II. EXPERIMENT

A. Suboxide molecular-beam epitaxy (*S*-MBE)

A molecular beam of TaO₂ is achieved by heating an iridium crucible containing Ta₂O₅ in an effusion cell heated to a temperature of about 1700 °C.²⁶ The calculated vapor pressures of species over Ta₂O₅ shows that the beam is dominated by the incongruent evaporation of the suboxide TaO₂ (see Figs. S1 and S2). The *S*-MBE approach avoids the notoriously unstable electron-beam evaporation of tantalum metal in conventional MBE and the need for subsequent oxidation using a background gas or plasma. The latter is particularly challenging to control in the quest for TaO₂ as the stable bulk phase of tantalum oxide is the 5d⁰ compound Ta₂O₅, a band insulator without an MIT, similar to the case of 3d⁰ V₂O₅ and 4d⁰ Nb₂O₅. In the *S*-MBE approach, Ta⁴⁺ is delivered to the substrate from a pre-oxidized molecular beam of TaO₂ and no additional oxidant such as oxygen or ozone background gas is required.

We have found that *S*-MBE of tantalum oxide benefits from the preparation of the oxide source material in the form of densely compacted pellets, as opposed to loose powders.²⁶ As a starting material, we purchased Ta₂O₅ powder from Alfa Aesar with a purity of 99.993 %. The high source temperatures (above 1700 °C) required to create a suitable flux of TaO₂ pose stringent demands on the crucible material. Here, we use iridium crucibles known for their thermal stability and resistance to oxidation. At 1750 °C, we achieve a growth rate around 10 nm h⁻¹. Unfortunately, such extreme temperatures significantly reduce the lifetime of high-temperature effusion cells. The chamber background pressure of the Veeco Gen10 system used for this study was \approx 5 \times 10⁻⁸ Torr during TaO₂ film growth and consisted mostly of oxygen (emanating from the Ta₂O₅ source).

Ta₂O₅ thin films were epitaxially grown on (111)-oriented yttria-stabilized zirconia (YSZ) substrates to act as a pentavalent tantalum oxide reference for X-ray and electron spectroscopy experiments. For Ta₂O₅ growth via *S*-MBE, distilled ozone was supplied to the center of the front side of the substrate via a water-cooled stainless steel nozzle and the background chamber pressure was kept at 1 \times 10⁻⁶ Torr.

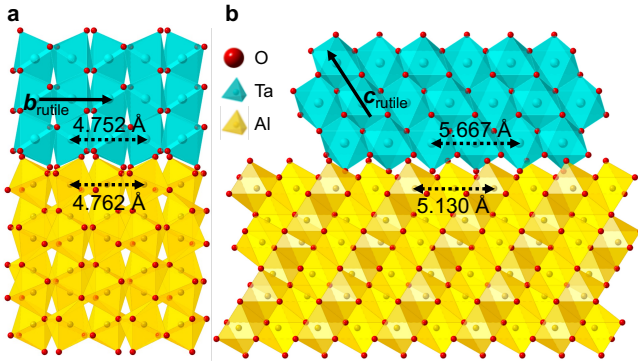
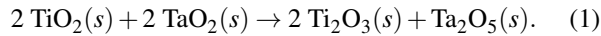


FIG. 1. Cross-sectional schematics of TaO₂ (101) (blue) on Al₂O₃ (112) (yellow) perpendicular to the rutile *b* and *c*-axes are shown in (a) and (b), respectively. The view direction into the plane for panel (a) is TaO₂ [101] || Al₂O₃ [1101] and for panel (b) is TaO₂ [010] || Al₂O₃ [1120].

We selected *r*-plane sapphire as the most promising substrate for TaO₂ film growth because it is stable under ultrahigh vacuum (UHV) conditions even at elevated substrate temperatures (*T*_{sub}) around 1000 °C that were found necessary to crystallize TaO₂. Figure 1 highlights the oxygen octahedral network of the film and substrate that continues across the heteroepitaxial interface. While one in-plane direction has an ideal fit along the rutile *b*-axis with only ≈ 0.2 % epitaxial strain, the orthogonal in-plane direction unfortunately suffers from a large misfit of ≈ 9.5 %. See supplementary material section S2 for calculation and discussion as well as a topview schematic (Fig. S3). We observe an epitaxial relationship for the growth of rutile TaO₂ on *r*-plane sapphire in the same way as Fukushima, Takaoka, and Yamada²⁷ reported it for rutile TiO₂ on *r*-plane sapphire.

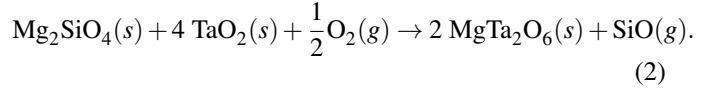
Of course, the ideal substrate for TaO₂ would have the rutile crystal structure itself. Unfortunately, both commercially available substrates with the rutile structure (TiO₂ and MgF₂) proved unsuitable for the synthesis of TaO₂. Unlike its 3*d*¹ analog VO₂, TaO₂ cannot conveniently be grown on abundantly available TiO₂ substrates due to the high *T*_{sub} required, around 1000 °C, which promotes the reduction of Ti⁴⁺. Attempts to grow TaO₂ on TiO₂ substrates led exclusively to Ta₂O₅ formation. This is consistent with Ellingham diagrams showing that at the oxygen partial pressure needed to stabilize Ta₂O₅, Ti₂O₃ (and not TiO₂) is stable.²⁸ This implies the reaction



Attempts to grow TaO₂ on MgF₂ were also unsuccessful due to the decomposition of the substrate at temperatures around 600 °C, well below the crystallization temperature of TaO₂ that was found to be around 1000 °C. The propensity of MgF₂ to oxidize and form a volatile fluoride gas during the growth of a metal oxide poses an additional challenge.²⁹

Preliminary attempts to grow TaO₂ on Mg₂SiO₄ (010) – a new substrate for rutile oxide heteroepitaxy that we re-

cently introduced²⁹ – resulted in the formation of MgTa₂O₆ and rough interfaces at substrate temperatures in the range of 1000–1200 °C. The proposed reaction is



The formation of MgTa₂O₆ resembles the findings of Sun, Senz, and Hesse³⁰ who reported the formation of MgTa₂O₆ when subjecting MgO (001) substrates to Ta-O vapors (from electron-beam evaporation of a Ta₂O₅ powder charge) at *T*_{sub} between 600–1000 °C and *p*O₂ = 7.5 × 10⁻⁵ Torr.

X-ray photoelectron spectroscopy (XPS) and scanning transmission electron microscopy (STEM) analysis showed that magnesium diffused from the substrate into the film and that tantalum was oxidized to its preferred pentavalent oxidation state. This observation motivates further research into the potential use of MgTa₂O₆ and related trirutiles as new substrates for the growth of rutile thin films with large lattice parameters.

As TaO₂ is not known to be a stable phase in the bulk, we initially capped films *in situ* with an amorphous layer of SiO_x at room temperature in ultrahigh vacuum before exposing the samples to ambient air. To this end, we used a pre-oxidized beam of silicon oxide emanating from a SiO charge (Alfa Aesar, 99.99 % purity).³¹ In later experiments, we found that TaO₂ films remain stable in air at room temperature for at least 1 year even without a capping layer such as amorphous SiO_x. All of the samples in this article were grown without a capping layer.

Before film growth, all substrates were sequentially cleaned in an ultrasonic bath using a series of solutions: a detergent solution ("Micro-90" (International Products Corporation (IPC)))³² in deionized water, pH ≈ 9.5), followed by acetone, and finally isopropyl alcohol, with each cleaning step lasting several minutes.

To heat to *T*_{sub} around 1000 °C during growth, we utilize a mid-infrared (10.6 μm) CO₂ laser-heating system built by epiray GmbH. The substrate temperature is monitored and controlled during growth via an on-axis infrared (7.5 μm) pyrometer. The pyrometer focus is projected through a ZnSe beam-splitter in the CO₂ shaping optics to target the bare substrate backside – the same incident surface as the CO₂ heating laser. The pyrometer reading is then fed into a PID loop for temperature control of the CO₂ laser output, resulting in a tight, stable laser output at fixed target temperatures across the full range from room temperature to 2000 °C both with and without continuous substrate rotation. To increase the accuracy of the temperature measurements despite partial attenuation of the 7.5 μm radiation through the laser beamline optics, we calibrate the system by intentionally melting the backside of a test Al₂O₃ substrate. This provides a known melting point (2054 ± 6 °C)³³ and substrate emissivity at 7.5 μm (≈ 1).³⁴ Assuming a true emissivity of 1, the ratio between the measured 7.5 μm radiation density and the known value for Al₂O₃ at the melting point represents the degree of 7.5 μm attenuation in the beam optics, which we find in our case to be ≈

0.55. Setting the pyrometer onboard electronics to an emissivity value matching this ratio then effectively compensates for the optical losses and provides substrate backside temperature readings across the full temperature range.

B. Thermal laser epitaxy (TLE)

Given the demanding deposition parameters required for the growth of epitaxial TaO₂ by MBE, alternative approaches merit consideration. In TLE, elemental sources are heated by continuous-wave lasers with a wavelength of $\approx 1 \mu\text{m}$ that is efficiently absorbed by most elements. Depending on the thermal properties of the element, the source material is either free-standing and self-contained or, if need be, placed in a crucible, from which it sublimates or evaporates to enable material transfer onto the substrate.^{35,36} The TLE system used in this work is equipped with the same CO₂-laser substrate heater as the aforementioned MBE system. Due to the unique mechanism of laser-based source heating and laser-based substrate heating, TLE offers a significantly broader process window than conventional epitaxial growth techniques.³⁷ This is particularly advantageous given the narrow and challenging conditions identified for the suboxide MBE growth of epitaxial TaO₂. Notably, tantalum has been established as a well-suited, free-standing source for TLE, and high deposition rates are readily attainable.¹⁷ To explore the parameter space in which TaO₂ may be grown by TLE, we applied a fixed source-laser power of 300 W. This resulted in a growth rate of $\approx 10 \text{ nm min}^{-1}$ for the parameter space shown in Fig. 2, grown on *c*-plane and *r*-plane sapphire. Note that this growth rate exceeds the suboxide MBE growth rate by over an order of magnitude. This allowed us to explore a wide range of T_{sub} and pressures for the growth of tantalum oxides. In the remainder of the article we focus on samples grown on *r*-plane sapphire, which enables untwinned growth of rutile, unlike *c*-plane sapphire.

Figure 2 summarizes the results from pressure and T_{sub} sweeps during TLE growth parameter optimization. At an oxygen partial pressure of 1.5×10^{-2} Torr, we identify a transition from the growth of epitaxial TaO₂ to Ta₂O₅. The formation of the desired epitaxial TaO₂ is observed for T_{sub} below 1200 °C and pressures between 3.75×10^{-3} Torr $< p_{\text{O}_2} < 1.5 \times 10^{-2}$ Torr. Among the TaO₂ samples, the XRD rocking curve full width at half maximum is narrowest for the film grown at $T_{\text{sub}} = 1200$ °C and widest for the sample grown at $T_{\text{sub}} = 800$ °C. At $T_{\text{sub}} > 1200$ °C, the films start to show metallic tantalum until $T_{\text{sub}} > 1400$ °C where only tantalum metal is observed. Conversely, at low T_{sub} and low oxygen pressures, the films become partially amorphous. The growth diagram in Fig. 2 indicates that the high tantalum flux achieved in TLE promotes the stabilization of the intermediate Ta⁴⁺ oxidation state. While the fully oxidized Ta⁵⁺ state is accessible under elevated oxygen partial pressures, the high tantalum flux in TLE likely exceeds the available oxidant supply within the regime where TaO₂ is formed. This imbalance between metal and oxygen flux limits complete oxidation, favoring the formation of the intermediate Ta⁴⁺ state. The emer-

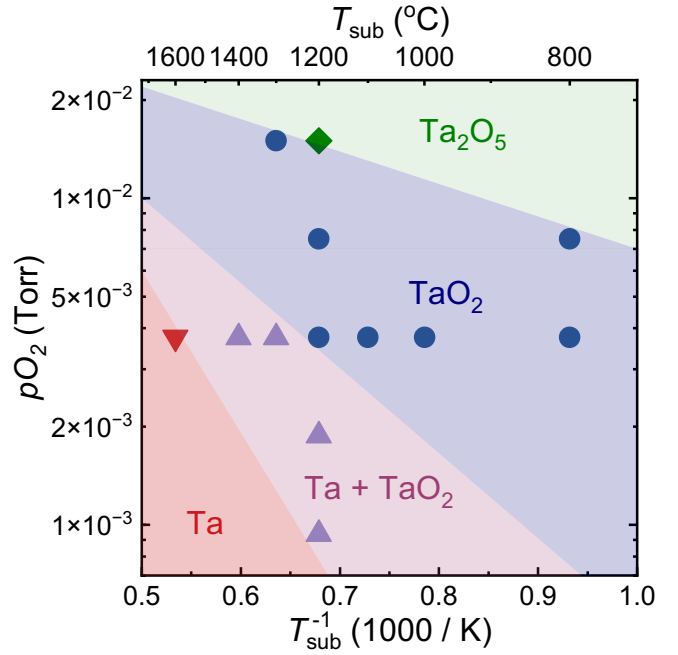


FIG. 2. Growth diagram summarizing the oxygen partial pressure (p_{O_2}) and substrate temperature (T_{sub}) dependence of the TLE growth of tantalum oxide. Phase-pure TaO₂ was obtained in the blue-shaded region of the diagram between 800 - 1300 °C. Scatter markers denote experimental data, colored backgrounds serve as guide to the eye.

gence of metallic tantalum at higher T_{sub} further supports this interpretation, as the diminished oxygen chemical potential at elevated T_{sub} reduces the system's capacity to fully oxidize the incoming metal flux.

Taken together, these observations underscore the delicate interplay between thermodynamic and kinetic factors in TLE. Nevertheless, we reproducibly identify a relatively broad window for the epitaxial growth of TaO₂ thin films using this technique.

C. Characterization

X-ray diffraction and reflectivity (XRD and XRR) measurements were performed using a PANalytical Empyrean diffractometer equipped with a hybrid 2-bounce germanium monochromator and a PIXcel3D detector. High-resolution rocking curves were measured using a germanium analyzer crystal on the diffracted beam side and a proportional counter. $\theta - 2\theta$ scans, rocking curves, and small two-dimensional (2D) reciprocal space maps (RSMs) were recorded using a $1/2^\circ$ divergence slit. For XRR, a narrow $1/32^\circ$ divergence slit was used. Three-dimensional (3D) X-ray reciprocal space mapping was performed at the QM^2 beamline at the Cornell High Energy Synchrotron Source (CHESS) at a beam energy of 15 keV using the protocol outlined by Wadehra *et al.*³⁸ 2D RSMs were extracted to show the film and substrate Bragg peaks in two representative orthogonal planes.

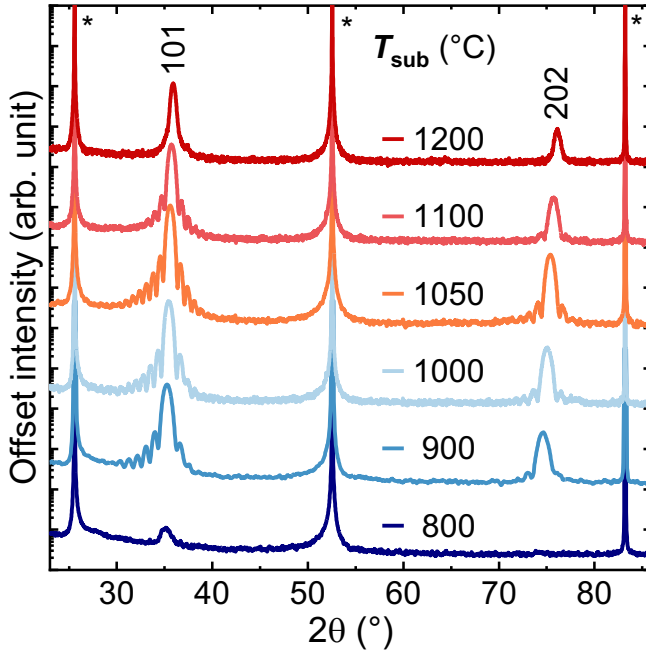


FIG. 3. X-ray diffraction of MBE-grown TaO₂ (101) thin film on Al₂O₃ (1102) scans showing pronounced Laue fringes for T_{sub} between 900 and 1100 °C. Peaks highlighted with an asterisk are due to the substrate.

Cross-sectional lamellae of MBE-grown TaO₂ films for STEM imaging and electron energy-loss spectroscopy (EELS) measurements were prepared with a Thermo Fisher Helios G4 UX focused ion beam. High-angle annular dark-field (HAADF) STEM imaging was performed on an FEI Titan Themis operated at 300 kV with a 21.4 mrad probe convergence semi-angle and 50 pA probe current. For high-precision structural measurements, a series of 40 rapid-frame images (0.4 s per frame) were acquired, aligned, and averaged with a rigid registration algorithm optimized to prevent lattice hops³⁹ to recover high signal, high fidelity atomic resolution images. EELS spectra were collected with a GIF Quantum ER spectrometer and a Gatan K2 Summit direct electron detector operated in counting mode. Four-dimensional (4D) STEM datasets for multislice electron ptychography were collected at 300 kV with a 21.4 mrad probe convergence angle, 46 mrad collection angle, and 50 pA probe current, scanning 256 × 256 points at a step size of 0.44 Å and dwell time of 100 μs on an EMPAD-G2 detector.⁴⁰ Multislice electron ptychography reconstructions were performed using the maximum likelihood algorithm⁴¹ implemented in the fold-slice package^{42,43} using multiple probe modes to account for partial coherence.^{41,44} Optimal reconstruction parameters were found with Bayesian optimization with an objective function minimizing the data error.⁴⁵

In situ non-monochromated XPS using a magnesium anode (1.3 keV) was performed at the PARADIM thin-film MBE-ARPES cluster at Cornell University. The sample was transferred from the growth chamber to the photoemission chamber at a pressure less than 5×10^{-8} Torr. Additional *ex situ*

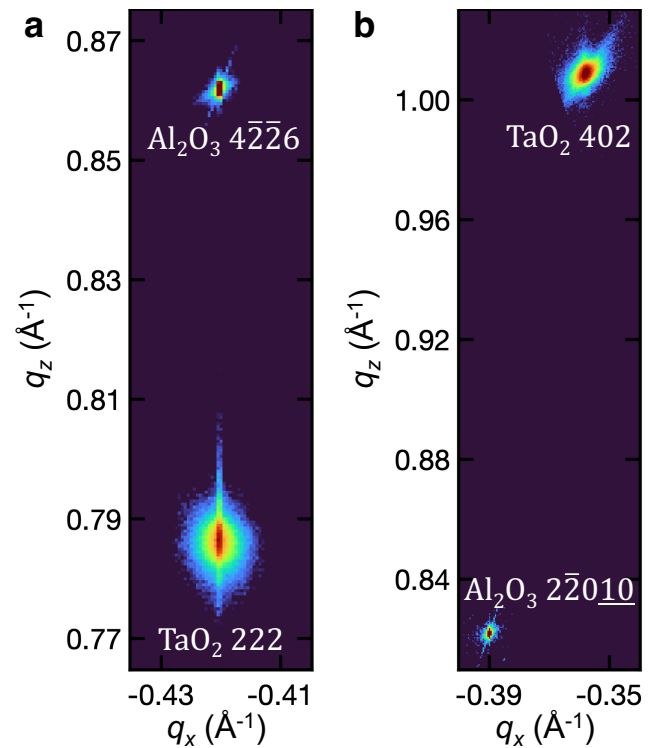


FIG. 4. XRD reciprocal space map revealing the anisotropic strain state of MBE-grown TaO₂ on Al₂O₃ (1102). Panel (a) shows that the film is commensurately strained to the substrate lattice parameter along the rutile *b* direction (see Fig. 1 for illustration); the film is fully relaxed in the orthogonal high-misfit direction (b).

XPS using a monochromated aluminum anode (1.5 keV) was performed using a ThermoFisher Nexsa G2 system with a 400 μm diameter spot size and a low-energy electron flood gun for charge neutralization. The pressure during the analysis was $\approx 1 \times 10^{-8}$ Torr, mostly argon gas. High-resolution spectra were collected at a pass energy of 40 eV and a step size of 0.1 eV. Survey spectra were recorded at a pass energy of 150 eV using a step size of 0.4 eV. To avoid unintentional reduction, the samples were not sputter-cleaned before analysis. The XPS data were analyzed using CasaXPS (v. 2.3.25).

To gain information of the interior of the film, hard X-ray photoemission spectroscopy (HAXPES) was performed on the tantalum 3d and 4f peaks using two different X-ray energies. Variable-temperature operando HAXPES was performed using a SPECS system at the University of Twente in the Netherlands⁴⁶ equipped with a chromium anode (5.4 keV) for the tantalum 4f peak, and a Scienta Omicron system equipped with a gallium (9.3 keV) liquid-metal-jet anode at Binghamton University, New York, for the tantalum 3d peak. Measurements of the tantalum 3d peaks show the same trends albeit less pronounced compared to the 4f peaks.

To investigate the stability of MBE-grown TaO₂ at elevated temperatures in vacuum using operando HAXPES, the sample was heated using a near-infrared laser shining on the backside of a blackened flag-style sample holder. The temperature was

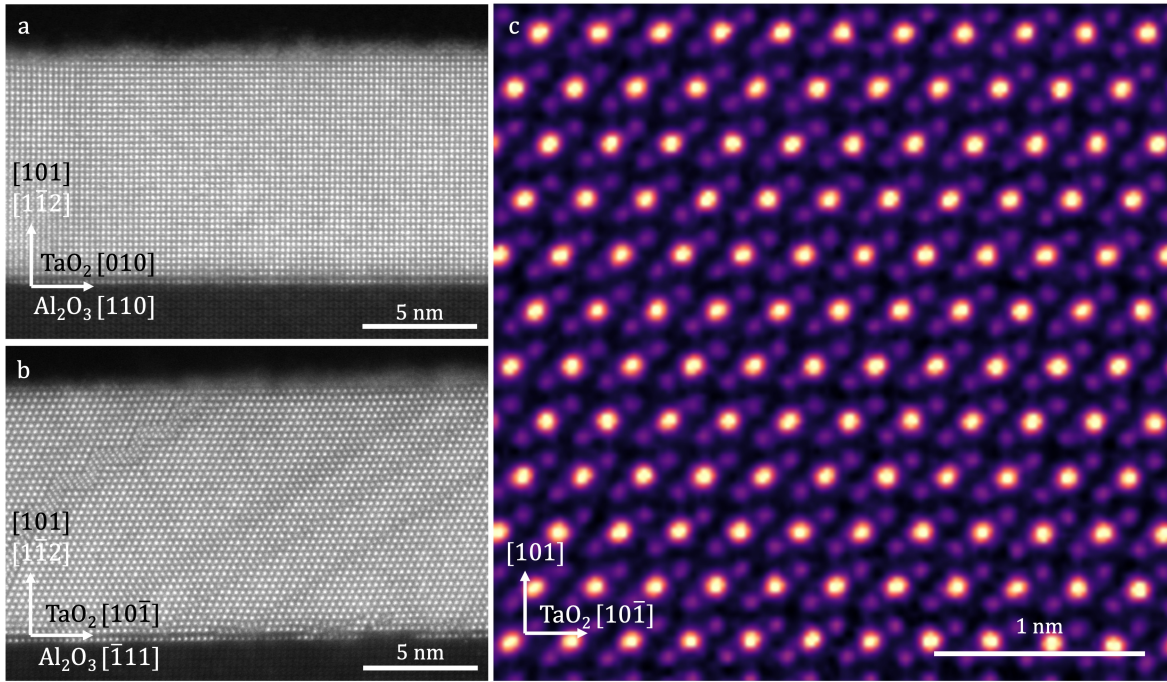


FIG. 5. Cross-sectional HAADF-STEM images of MBE-grown TaO₂ taken (a) perpendicular and (b) parallel to the rutile *b*-axis. In panel (a), the film appears commensurately strained, as evidenced by the perfect alignment between tantalum ions in the film and aluminum ions in the substrate. In contrast, panel (b) reveals diagonal striations and an incommensurate interface marked by numerous dislocations. Panel (c) presents a magnified view of a defect-free region in the same orientation as (b), reconstructed using multislice electron ptychography to simultaneously resolve tantalum (depicted in yellow) and oxygen (purple) atomic columns.

monitored using a thermocouple spot-welded onto the sample plate. The pressure in the analysis chamber was on the order of 1×10^{-8} Torr and spiked briefly during each heating step, likely due to the outgassing of the silver paint used to mount the sample on the flag-style holder. Residual gas analysis indicated that the background gas consisted mostly of H₂O and O₂.

Oxygen *K*-edge XAS was performed at the *Versox* beamline at Diamond Light Source.⁴⁷ The signal was collected in total electron yield (TEY) mode by measuring the drain current from the sample holder. The highly insulating nature of film and substrate led to highly distorted spectra with curved backgrounds. Attempts to record and analyze the tantalum *N*-edges were unsuccessful due to their broad and weak nature. Tantalum *L*₃ edge measurements were performed at the *PIPOXS* beamline at CHESS in partial fluorescence yield (PFY) mode. The incident beam was energy selected using a Si(111) monochromator and reflected off two rhodium-coated mirrors set to 4 mrad for harmonic rejection. Tantalum metal foil was measured in transmission geometry using N₂-filled ion chambers while TaO₂ and Ta₂O₅ thin films were placed at 45° relative to the incident beam and signal detected using a four element Vortex detector.

We studied resonant inelastic X-ray scattering (RIXS) at the tantalum *L*₃ edge at beamline ID20 of the European Synchrotron Radiation Facility. Photons from three consecutive U26 undulators were monochromatized by a Si(111) high-heat-load monochromator and a successive Si(311) channel

cut monochromator. Using a spectrometer in Rowland geometry with a spherically shaped diced Si(660) analyzer crystal (1 m radius of curvature), we achieved an overall energy resolution of 300 meV. All measurements were performed at 300 K. RIXS is a photon-hungry technique. To enhance the RIXS signal for measurements on a TLE-grown thin film with a thickness of 43 nm, we utilized a grazing incident angle $\theta = 1^\circ$ that maximizes absorption within the thin film and a scattering angle 2θ close to 90° that minimizes self-absorption.

Spectroscopic ellipsometry measurements were performed on MBE-grown epitaxial TaO₂ (≈ 82 nm) on *r*-plane Al₂O₃ to determine the complex dielectric function ($\epsilon = \epsilon_1 + i\epsilon_2$) spectra of epitaxial TaO₂. The thickness determined by modeling of the ellipsometry data was independently verified by fitting X-ray reflectivity measurements (not shown). Reference measurements were performed on an uncoated *r*-plane sapphire substrate (see supplementary material). Generalized ellipsometric spectra were collected at 40, 45, and 50° angles of incidence in the 0.225 – 0.50 eV photon energy range using a rotating compensator Fourier transform infrared (IR) ellipsometer (FTIR-VASE, J.A. Woollam Co.)⁴⁸ and in the 0.50 – 4.13 eV photon energy range using a single-channel rotating-analyzer ellipsometer with an auto-retarder (V-VASE, J.A. Woollam Co.).^{49,50} Generalized ellipsometric spectra are collected at four different sample orientations varying the azimuthal Euler angle ϕ with both ellipsometers to determine the structural and optical properties of the epitaxial TaO₂ film. The optical properties of Al₂O₃ are fixed from the measure-

ment of the uncoated *r*-plane Al₂O₃. The polar Euler angle θ for TaO₂ is fixed to 33.8° which is the angle between the *c*-axis and the (101) surface plane of the TaO₂ film. Details are provided in Sec. S11 in the supplementary material.

Atomic force microscopy images were recorded *ex situ* in air at room temperature using an Asylum Research Cypher S instrument with NanoWorld Arrow-UHFAuD-10 cantilever probes. Post-processing was performed using Gwyddion (v.2.67). Figure S4 shows a series of topography images. While the film appears to grow as small islands, the underlying step-and-terrace morphology of the *r*-plane sapphire substrate remains clearly visible.

III. RESULTS AND DISCUSSION

A. X-ray diffraction

XRD results in Fig. 3 demonstrate that phase-pure TaO₂ can be grown by suboxide MBE over a wide T_{sub} range from 800–1200 °C. The exclusive presence of peaks arising from the (101) plane attests to the single out-of-plane orientation. The experimental lattice parameters are $a = 4.66(2)$, $b = 4.76(2)$, $c = 2.99(1)$ Å. XRD ϕ -scans (see Fig. S5) confirm the untwinned nature of these films. The epitaxial growth is further corroborated by the streaky reflection high-energy electron diffraction (RHEED) pattern shown in Fig. S6.

Figure 4 shows X-ray reciprocal space maps (RSMs) that probe two orthogonal in-plane directions, corresponding to the schematic depicted in Fig. 1. The data reveals the highly anisotropic nature of TaO₂ (101) on Al₂O₃ (1102). This is consistent with the surface unit cell of the substrate, see Fig. S3. The epitaxial mismatch along the [010]_R direction (subscript *R* denotes the rutile unit cell) is about 0.2% (tensile strain), whereas in the [101]_R direction, it is about –9.5% (compressive strain). This results in the film being pseudomorphic only in the [010]_R direction. In the orthogonal direction, the film is relaxed from the substrate-film interface and shows periodic defects.

Large field-of-view synchrotron X-ray RSMs are shown together with diffraction simulations in the supplementary material in Fig. S7 and confirm the untwinned, single-oriented growth of rutile TaO₂ on *r*-plane sapphire. High-temperature XRD data (Fig. S8) reveal that TaO₂ irreversibly oxidizes to Ta₂O₅ around 400 °C in air.

B. Scanning transmission electron microscopy

Atomic resolution HAADF-STEM images were collected on two orthogonal cross-sections of the film, the rutile [101] and [010] zone axes, revealing its anisotropic structure. Along the [101] zone axis, the tantalum sublattice visible with HAADF-STEM shows good agreement with a rutile polytype, and is fully strained along the [010] direction with a low density of defects. On the other hand, along the [010] zone axis a high density of diagonal striations perpendicular to the rutile *c*-axis is present, accomodating a relaxation of the film at

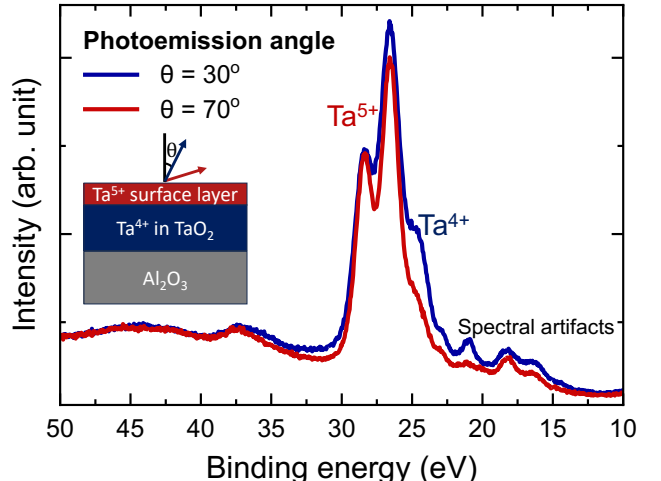


FIG. 6. Tantalum 4f X-ray photoemission spectroscopy data of MBE-grown TaO₂ collected *in situ* at two different photoemission angles using a non-monochromatic magnesium anode. The inset depicts a cross-sectional model of the sample.

the interface along the [101] direction due to the large misfit strain with the Al₂O₃ substrate. While conventional HAADF-STEM imaging readily resolves the film's cation sites and relevant symmetries and defects, it lacks the sensitivity to measure the arrangement of oxygen ions in the material.

To confirm the film's rutile structure, multislice electron ptychography was used to fully characterize both the tantalum and oxygen sublattices, revealing the edge- and corner-sharing octahedra characteristic of the rutile structure, which is maintained even across the dense defects visible along the [101] zone axis. Thus, the combination of HAADF-STEM imaging and electron ptychography shows that the film exhibits a distorted rutile structure, with inequivalent *a* and *b* lattice parameters, and highly oriented defects associated with a partially relaxed, anisotropic epitaxial strain state.

C. X-ray photoemission spectroscopy

Figure 6 shows XPS data collected *in situ* on an MBE-grown TaO₂ thin film (≈ 10 nm) before exposure to ambient air. Tantalum 4f XPS data were collected at two different photoemission angles, providing information from different probing depths. In the more surface-sensitive high photoemission angle geometry, the data looks Ta⁵⁺-like. At low photoemission angle, however, a strong shoulder appears on the lower binding energy side of the tantalum 4f_{7/2} peak, around 24 eV, indicative of a reduced valence state which we assign to Ta⁴⁺. In summary, the XPS data points towards the formation of a pentavalent overlayer on top of the tetravalent TaO₂. Muraoka *et al.*²⁵ reported a similar result and estimated an overlayer thickness of 3 nm of unintentional Ta₂O₅-like crust. The formation of an oxidized surface layer was previously described for the structurally and electronically similar oxides VO₂^{51,52} and NbO₂⁵³ as well. We cautiously conclude that the surface

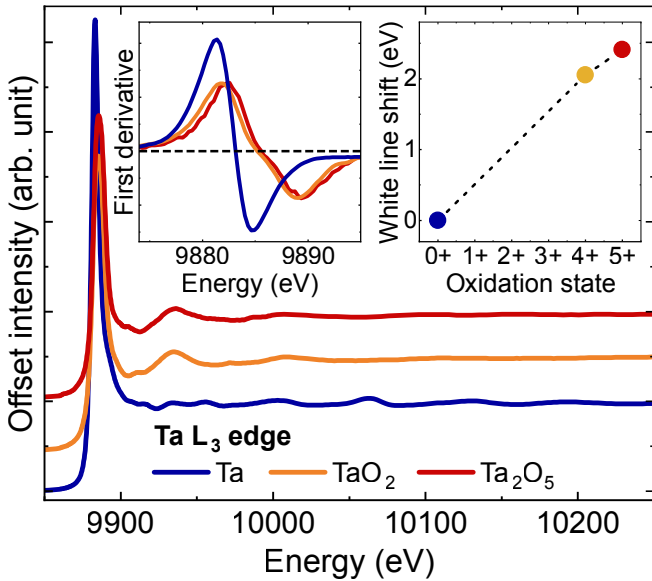


FIG. 7. Tantalum L_3 X-ray absorption spectroscopy of MBE-grown TaO_2 . The insets show the derivative of the white line (left) and the white-line shift against the formal oxidation state of tantalum, TaO_2 , and Ta_2O_5 (right) as determined from the root of the derivative.

oxidation is self-limiting as we observed no aging effects of the samples during the course of two years of exposure to air when comparing XRD data.

To enhance the experimental sensitivity for the buried tetravalent TaO_2 layer, we next turn to hard X-ray photoemission spectroscopy (HAXPES). Figure S9 shows a comparison of TaO_2 and Ta_2O_5 data. Our Ta_2O_5 data are in excellent agreement with HAXPES reference spectra that were recently published by Zheng *et al.*⁵⁴ For TaO_2 , we observe the asymmetric peaks of the Ta^{5+} doublet with pronounced shoulders on the lower binding energy side, indicative of a reduced valence state compared to Ta^{5+} .

We performed operando HAXPES measurements to test the high-temperature stability of TaO_2 thin films in UHV (pressure $< 1 \times 10^{-8}$ Torr). Figure S10 shows *ex situ* HAXPES data at elevated temperatures. Up to $\approx 700^\circ\text{C}$, the HAXPES spectra look identical to the room-temperature ones. Around 900°C , an irreversible oxidation reaction took place, fully transforming TaO_2 into Ta_2O_5 . This is evidenced by the disappearance of the small density of states near the Fermi level observed for TaO_2 as well as the $\text{Ta}^{4+} 4f_{7/2}$ peak near 24 eV binding energy. This oxidation is remarkable as most oxide thin films tend to reduce in UHV conditions at elevated temperatures and emphasizes the challenge of stabilizing tetravalent tantalum in TaO_2 .⁵⁵

D. X-ray absorption spectroscopy

The oxygen K -edge of our MBE-grown TaO_2 thin films (not shown) resembles spectra of Ta_2O_5 . We note that in the TEY mode, the experiment is sensitive only to the top few

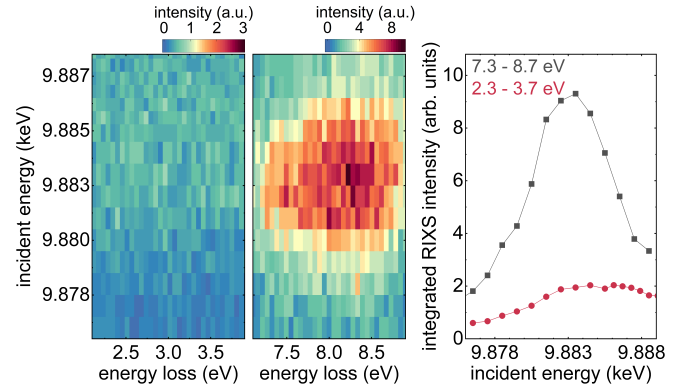


FIG. 8. Resonance behavior of tantalum L_3 -edge RIXS of a TLE-grown TaO_2 film. Left and middle: RIXS intensity as function of the incident energy for energy loss around 3 and 8 eV, respectively. Note the different color scales. Right: integrated RIXS intensity for the energy windows shown in the other panels. We observe a charge-transfer peak at about 8 eV energy loss but no spectral feature at lower energies.

nanometers of the specimen. This therefore corroborates the presence of a pentavalent tantalum oxide overlayer on the surface of TaO_2 revealed by XPS. To obtain more information about the interior of the TaO_2 film, we next turned to a bulk-sensitive hard X-ray measurement, namely the tantalum L_3 edge, which probes $2p_{3/2} \rightarrow 5d$ transitions. Fig. 7 shows a comparison of TaO_2 with tantalum metal and Ta_2O_5 absorption spectra. In rutile TaO_2 , tantalum ions are coordinated octahedrally with oxygen ions. This is also true for most tantalum ions in Ta_2O_5 except those that are in a pentagonal bipyramidal (TaO_7 unit). This similarity in coordination is the reason why the EXAFS signal of the TaO_2 and Ta_2O_5 thin films appear qualitatively very similar. We acknowledge that our EXAFS data is noisy, as is often the case for thin films measured in the fluorescence yield mode, and therefore we refrain from a detailed analysis. Instead, we focus on the strong white line and its energy shift with the expected oxidation state. We determine the position of the white line using the roots of the first derivative (see left inset). The peak position for TaO_2 falls in between tantalum metal and the pentavalent Ta_2O_5 reference samples.

E. Resonant inelastic X-ray scattering

To further investigate the elusive $5d^1$ electronic structure, we attempted resonant inelastic X-ray scattering (RIXS) at the tantalum L_3 edge on a TaO_2 sample grown by TLE. The RIXS process consists of an initial X-ray absorption step in which a $2p$ core electron is promoted into the $5d$ shell. Then, the corresponding $2p$ core hole is filled by a valence electron, leaving the system in a low-energy excited state. In the case of a Mott insulator with a $5d^1$ configuration, the absorption into the $5d$ shell boosts spin and orbital excitations.⁵⁶ More precisely, one expects to observe the excitation from a local, spin-orbit-driven $j=3/2$ ground state to a $j=1/2$ excited state

at low energy and excitations from t_{2g} to e_g orbitals at roughly 3 eV, as reported for Rb₂TaCl₆ with 5d¹ Ta⁴⁺ ions in an octahedral ligand cage.⁵⁷ Therefore, RIXS is an excellent tool to determine the local electronic structure. A further motivation was to search for a possible dimerization at low temperature and in analogy to the case of VO₂. Hard X-ray L -edge RIXS can detect such a superstructure via the corresponding interference pattern in the RIXS intensity, as observed, e.g., for dimers in iridates or, at the tantalum L_3 edge, for tetrahedra in the lacunar spinel GaTa₄Se₈.^{58,59}

We studied the resonance behavior, i.e., the RIXS intensity for different incident energies E_{in} across the tantalum L_3 edge; see Fig. 8. We find a pronounced charge-transfer peak at about 8 eV energy loss which is resonantly enhanced at E_{in} about 9.883 keV. Nevertheless, for energy loss between 2 and 4 eV – note the different color scale – the data do not show the t_{2g} - e_g excitations expected for a 5d¹ compound. This suggests a 5d⁰ state that allows for charge-transfer excitations, but not for d - d excitations, as reported for 5d⁰ SrLaMgTaO₆.⁶⁰ Unfortunately, the sample immediately degraded under the intense X-ray beam, showing clear visual signatures of radiation damage. At present, the RIXS result is inconclusive as to whether the sample is indeed a 5d⁰ tantalum oxide or whether the elusive 5d¹ state also rapidly decays under the beam. There remains hope that samples with a higher structural quality and deliberate capping layers will exhibit greater stability and spectral cleanliness. Success for such an endeavor necessitates better lattice matched substrates and is motivation for future work into the design of new substrates for oxides with the rutile structure.

F. Electron energy-loss spectroscopy

To spectroscopically investigate the interior of the TaO₂ thin film, we prepared a cross-sectional lamella using focused-ion beam milling. Because the tantalum $N_{2,3}$ edges are weak and broad, we focus on the oxygen K -edge instead. The EELS data are presented in Fig. S11, where they are also compared to a pentavalent tantalum oxide reference. To qualitatively guide our expectations, we computed the oxygen K -edges on the DFT-LDA level. The key difference between TaO₂ and Ta₂O₅ is the ratio between the first two peaks. This part of the oxygen K -edge is sensitive to the tantalum 5d orbitals due to oxygen 2p - tantalum 5d hybridization. Qualitatively, the first peak is expected to be larger for Ta₂O₅ because the latter has an empty 5d – t_{2g} manifold. This is in contrast to TaO₂ which has 1 electron in the 5d orbital. See supplementary material for a comparison between the experimental data and DFT-based calculated spectra (see Fig. S12).

G. Spectroscopic ellipsometry

The directionally dependent complex dielectric function ($\epsilon = \epsilon_1 + i\epsilon_2$) spectra of an 82 nm thick MBE-grown TaO₂ thin film were determined from generalized spectroscopic el-

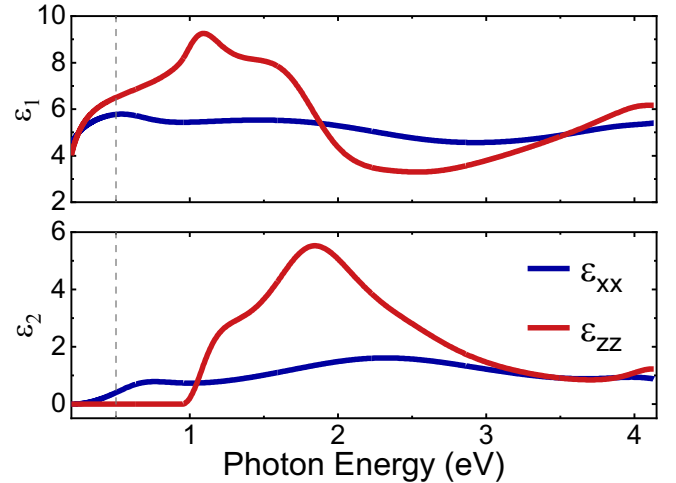


FIG. 9. Real (ϵ_1) and imaginary (ϵ_2) parts of the complex dielectric function determined from spectroscopic ellipsometry measurements in the ordinary (ϵ_{xx}) and extraordinary (ϵ_{zz}) directions. The dotted line indicates the transition between two different instruments.

lipsometry measurements and are depicted in Fig. 9. Measurements on a bare Al₂O₃ substrate are shown in Fig. S13.

Crystals with a rutile structure exhibit uniaxial birefringence, meaning that the optical response depends on the orientation of the incident light's wavevector \mathbf{k} relative to the crystal's optic axis, the rutile c -axis. The ordinary response ϵ_{xx} occurs when the electric field \mathbf{E} is entirely perpendicular to the optic axis ($\mathbf{E} \perp c$); in this case, light experiences the ordinary refractive index n_o . The extraordinary response ϵ_{zz} occurs when \mathbf{E} has a component parallel to the optic axis; in this case, the effective refractive index n_e depends on the angle between the wavevector and the optic axis. For (101)-oriented rutile films, the optic axis is inclined relative to the surface. In TaO₂, the angle between the (001) and (101) planes is 33.8°, see Fig. 1 (b) for illustration. The strong anisotropy in the complex dielectric function spectra (Fig. 9) agrees with the rutile crystal structure. Factors that are not captured in the analysis of the ellipsometry data are possible compositional gradients in the film due to the surface oxidation of TaO₂ as well as the anisotropic strain and the resulting defects.

For ease of comparison with the literature, the imaginary part of the permittivity was converted to the real part of the optical conductivity and displayed in Fig. S15. In particular the strength of the peaks below 3 eV are consistent with values reported for other Mott insulators, such as 3d, 4d, 5d transition metal compounds.^{61–65} In contrast, a clean d^0 system would have no optical transitions below the charge-transfer gap. While defects in a d^0 compound would yield d^1 states with similar energies to the ones reported here, the contribution of such defect states to the optical conductivity is expected to be weaker than the excitations across the Mott-Hubbard gap from $|d^1d^1\rangle$ to $|d^0d^2\rangle$, which are typically on the order of a few 100 $\Omega^{-1} \text{cm}^{-1}$. For comparison, the bandgap of Ta₂O₅ is ≈ 4 eV and there are no absorption features at lower energies.^{66,67} The absorption coefficient α is provided in Fig. S16. The smallest direct and indirect optical transitions of

our TaO₂ film are extracted via Tauc plots of $(\alpha h\nu)^{1/2}$ and $(\alpha h\nu)^2$, respectively (see Figs. S17 and S18). The transition occurring at the lowest photon energy is observed in the ordinary direction and is considered to be indirect. We therefore determine the optical bandgap of TaO₂ to be ≈ 0.3 eV.

H. Electrical transport

We attempted to measure the DC resistance-temperature relationship of MBE-grown TaO₂ thin films above room temperature. To this end, we built a custom setup using an evacuated Fine Instruments tube furnace. The temperature was measured with a K-type thermocouple using a Keithley 740 thermometer. The resistance was measured using the linear four-probe method using a Keithley 196 digital multimeter. Kanthal wires were glued to sputtered chromium contacts on the surface of the tested layer with Dupont 6838 high-temperature conductive silver paste. The sample was mounted on an alumina support. Despite best efforts, the resistance of all tested samples exceeded the measurement range near room temperature and was limited by setup leakage at high temperatures.

We expected to measure strongly anisotropic electrical transport properties, given the dislocations and periodic defects in one direction and high degree of structural quality in the commensurately strained direction. In contrast to our expectations, we find the resistance in both directions to exceed our measurement capabilities ($> G\Omega$).

The oxidized surface layer on top of TaO₂ poses a challenge to the fabrication of ohmic contacts and might act as a wide-gap tunnel barrier. In an attempt to reduce the effective Schottky barrier effect of the oxidized surface layer, we used a shadow mask process to pattern mm-sized contacts. To this end, we locally sputter-cleaned and gently reduced the surface layer of a TaO₂ thin film before Ti-Pt deposition via magnetron sputtering. Unfortunately, four-probe resistance measurements remained out-of-range. We therefore speculate that the carriers in TaO₂ are highly localized.

Preliminary attempts to chemically dope TaO₂ with magnesium concentrations of up to 20 % did not result in a measurable reduction of the electrical resistance and produced no discernible changes in the XRD θ - 2θ scans. Magnesium was selected as a dopant because of its stable valence and because Mg²⁺ has an ionic radius within 6 % of that of octahedrally coordinated Ta⁴⁺.⁶⁸ Subsequent growth experiments of TaO₂ on Mg₂SiO₄ substrates revealed the unintentional formation of MgTa₂O₆, a d^0 compound. The propensity to form this phase may account for the ineffectiveness of magnesium doping in TaO₂.

IV. FIRST-PRINCIPLES CALCULATIONS

First-principles density-functional theory calculations were used to evaluate the structural, electronic, and dielectric properties of TaO₂, assuming an infinite, strain-free periodic crystal. The computational details and results are discussed in section S12 of the supplementary material. Two phases of TaO₂

were thoroughly investigated: the high-symmetry rutile-like $P4_2/mnm$ structure (space group #136) and a lower-symmetry $I4_1/a$ structure (space group #88), which had a lower total energy. The transition from $P4_2/mnm$ to $I4_1/a$ is the result of a phonon at the R -point condensing into the $P4_2/mnm$ structure and matches with the expectation of the experimentally observed transition in NbO₂, the $4d^1$ analog of TaO₂.^{4,5} Our calculations show that whereas the $P4_2/mnm$ phase of TaO₂ is consistently metallic, the properties of the $I4_1/a$ phase are sensitive to the value of an applied Hubbard U term on the Ta- d states. Notably, there exists an energetic barrier between the two phases at $U = 0$ eV which vanishes as U approaches 4 eV. Additionally, the $I4_1/a$ phase transitions from being conducting at $U = 0$ eV to insulating as U increases, with an indirect band gap of ≈ 0.7 eV and a direct gap of ≈ 1 eV. The direct bandgap (≈ 1 eV) is in excellent agreement with that obtained by spectroscopic ellipsometry. Furthermore, both techniques find a smaller indirect bandgap, albeit with different energies (ellipsometry ≈ 0.3 eV, DFT ≈ 0.7 eV).

Figures S23, S24, S27, S28 in the supplementary material show relative permittivity spectra computed from first principles using various values of the Hubbard U parameter and three different exchange-correlation functionals for the undistorted rutile polymorph of TaO₂ ($P4_2/mnm$) as well as the NbO₂-like ($I4_1/a$) polymorph. Although there are some differences between the computational and experimentally measured spectra, the spectra of the distorted $I4_1/a$ polymorph qualitatively match the experimental complex permittivities irrespective of the exact value of U and for all three exchange-correlation functionals. In summary, our computational results for $5d^1$ TaO₂ approximately capture both the bandgap energy as well as the peak energies.

V. CONCLUSION

In summary, we show that *r*-plane sapphire is a chemically stable substrate for the growth of TaO₂. Unlike *c*-plane sapphire, *r*-plane enables the growth of single-domain, untwinned rutile TaO₂ thin films. Using X-ray, optical, and electron spectroscopies, we characterize the metastable $5d^1$ electron configuration of tantalum in the interior of TaO₂ thin films and detect the presence of an oxidized surface layer. In contrast to an earlier report,²⁵ we demonstrate direct heteroepitaxy of TaO₂ without the need for a dedicated template or buffer layer and we show that this result is attainable using two deposition techniques, namely S-MBE and TLE. First-principles calculations support the existence of the rutile phase and reveal a ground state with a NbO₂-like distortion. While the calculations suggest that the undistorted rutile polymorph would be metallic, all samples in this study are highly electrically insulating with a ≈ 0.3 eV optical bandgap in rough agreement with calculated dielectric spectra for the distorted phase. The prediction of two competing phases close in energy motivates further studies of a possible metal-insulator phase transition between them analogous to the archetypic case of VO₂.

Despite best efforts, experimental signatures of a metal-

insulator transition in this 5d¹ compound have so far remained elusive. We speculate that higher-quality samples with fewer structural defects are needed to unlock the intrinsic properties of notoriously hard to stabilize TaO₂. This hinges on the availability of suitable substrates with a better lattice match. In our future work, we will explore the growth of trirutile MgTa₂O₆ and columbite MgNb₂O₆ as candidate substrates. Preliminary tests using olivine Mg₂SiO₄ as a candidate substrate for high-temperature rutile film growth led to decomposition and intermixing at the interface and unintentional MgTa₂O₆ formation.

VI. SUPPLEMENTARY MATERIAL

ACKNOWLEDGMENTS

This work was primarily supported by U.S. Department of Energy, Office of Science, Office of Basic Energy Sciences, under Contract No. DE-SC0019414 (thin film synthesis: A.S.P., Y.A.B., D.G.S.; X-ray experiments and interpretation Y.A.B., B.Z.G, A.S.; first-principles theory: J.Z.K. and N.A.B.).

The authors thank Yibin Bu for performing preliminary HAXPES measurements, Mark Pfeifer for technical assistance with the high-temperature XRD, and Steven Button for substrate preparation. The authors thank Qijun Che, Jelle Ruiter, Koen M. Draijer for support during synchrotron beamtimes, Shun-Li Shang for providing vapor pressure calculations, and Jochen Mannhart for supporting the TLE.

This work made use of the synthesis and electron microscopy facilities of the Platform for the Accelerated Realization, Analysis, and Discovery of Interface Materials (PARADIM), which are supported by the NSF under Cooperative Agreement No. DMR-2039380. This work made use of the Cornell Center for Materials Characterization shared instrumentation facility. The FEI Titan Themis 300 was acquired through NSF-MRI-1429155, with additional support from Cornell University, the Weill Institute, and the Kavli Institute at Cornell. The Helios FIB was acquired with support by NSF DMR-2039380. This work entails research conducted at the Center for High-Energy X-ray Sciences (CHEXS), which is supported by the National Science Foundation (BIO, ENG and MPS Directorates) under award DMR-2342336. This research was funded, in part, by the Gordon and Betty Moore Foundation's EPiQS Initiative (Grant nos. GBMF3850 and GBMF9073) to Cornell University. The authors acknowledge the European Synchrotron Radiation Facility (ESRF) for provision of synchrotron radiation facilities under proposal number BLC-15590 and thank K. Ruotsalainen, B. Detlefs, and C. Sahle for assistance and support in using beamline ID20. This publication is part of the project *Conductivity on demand – turning an insulator into a metal* with project number 019.223EN.017 of the research program RUBICON, which is partly financed by the Dutch Research Council (NWO). Part of this research was carried out at the MESA+ operando HAXPES user facility at the University of Twente. This publication is part of the project "Lab-based HAXPES facility for operando studies of energy-

material interfaces" with file number 175.2019.001 of the research programme NWO-groot 2019/2020 which is partly financed by the Dutch Research Council (NWO). N.A. thanks Utrecht University for a start-up grant (Dutch Sector Plan) supporting this work. E.B. and M.G. acknowledge funding from the Deutsche Forschungsgemeinschaft (DFG, German Research Foundation) through Project No. 277146847-CRC 1238 (B03). The work at AGH University was supported by the National Science Centre, Poland, Grant OPUS No. UMO2021/41/B/ST3/03454. Computational resources were provided by the Cornell Center for Advanced Computing. The authors thank Turan Birol for helpful discussions regarding the computational results.

VII. AUTHOR DECLARATIONS

A. Conflict of Interest

The authors F.V.E.H and D.G.S. have been granted U.S. Patent No. 11,462,402 (4 October 2022) with the title "Sub-oxide Molecular-Beam Epitaxy and Related Structures." The author B.D.F. is an employee of epiray GmbH, a company that sells commercial CO₂ laser heater and TLE systems.

B. Author contributions

Y.A.B. and A.S.P. contributed equally. Y.A.B. conceived the project and fabricated the samples together with A.S.P. under the guidance of M.R.B. and D.G.S. T.S. prepared the Ta₂O₅ source rods and fabricated supplementary TaO₂ and Ta₂O₅ samples. F.V.E.H. performed the TLE. N.S. performed the STEM analysis with guidance from D.A.M. J.Z.K. performed the DFT calculations with guidance from N.A.B. Y.A.B. and B.Z.G. performed the synchrotron XRD with guidance from S.S. and A.S. Y.A.B. and T.A.K. performed and analyzed the AFM. Y.A.B, I.C.G.B., E.M.K., and C.J.P. performed the XAS with guidance from F.M.F.G. E.B. and M.G. performed the RIXS at ESRF. Y.A.B and I.C.G.B performed the operando HAXPES with guidance from C.B. B.D.F. and M.J.W. performed additional XPS and HAXPES. A.B. and S.C. performed the ellipsometry with guidance from N.J.P. W.T and W.T. performed the resistance measurements. N.A. performed the DFT-based XAS calculations. Y.A.B. wrote the manuscript with input from all authors.

DATA AVAILABILITY STATEMENT

The data that support the findings of this study are openly available at

¹M. Imada, A. Fujimori, and Y. Tokura, "Metal-insulator transitions," *Rev. Mod. Phys.* **70** (1998).

²L. E. Noskin, A. Seidner, and D. G. Schlom, "Growth of NbO₂ by molecular-beam epitaxy and characterization of its metal-insulator transition," in *MRS Advances*, Vol. 2 (Materials Research Society, 2017) pp. 3031–3036.

³F. J. Morin, "Oxides which show a metal-to-insulator transition at the Néel temperature," *Physical Review Letters* **3**, 34–36 (1959).

⁴R. F. Jannink and D. H. Whitmore, "Electrical conductivity and thermoelectric power of niobium dioxide," *J. Phys. Chem. Solids* **27**, 1183–1187 (1966).

⁵G. Bélanger, J. Destry, G. Perluzzo, and P. M. Raccah, "Electron transport in single crystals of niobium dioxide," *Canadian Journal of Physics* **52**, 2272–2280 (1974).

⁶J. L. Hart, S. Siddique, N. Schnitzer, S. D. Funni, L. F. Kourkoutis, and J. J. Cha, "In operando cryo-STEM of pulse-induced charge density wave switching in TaS₂," *Nature Communications* **14** (2023), 10.1038/s41467-023-44093-2.

⁷E. Navarro-Moratalla, J. O. Island, S. Manás-Valero, E. Pinilla-Cienfuegos, A. Castellanos-Gómez, J. Quereda, G. Rubio-Bollinger, L. Chirrolli, J. A. Silva-Guillén, N. Agrait, G. A. Steele, F. Guinea, H. S. V. D. Zant, and E. Coronado, "Enhanced superconductivity in atomically thin tas₂," *Nature Communications* **7** (2016), 10.1038/ncomms11043.

⁸B. Sipos, A. F. Kusmartseva, A. Akrap, H. Berger, L. Forró, and E. Türi, "From Mott state to superconductivity in 1T-TaS₂," *Nature Materials* **7**, 960–965 (2008).

⁹M. H. V. Maaren and G. M. Schaeffer, "Some new superconducting Group Va dichalcogenides," *Physics Letters* **24**, 305 (1967).

¹⁰R. Venturini, A. Mraz, I. Vaskivskyi, Y. Vaskivskyi, D. Svetin, T. Mertelj, L. Pavlović, J. Cheng, G. Chen, P. Amarasinghe, S. B. Qadri, S. B. Trivedi, R. Sobolewski, and D. Mihailovic, "Ultraefficient resistance switching between charge ordered phases in 1T-TaS₂ with a single picosecond electrical pulse," *Applied Physics Letters* **120** (2022), 10.1063/5.0096850.

¹¹M. Huber, S. Zuber, V. Rosa-Rocha, S. C. Haley, N. Dale, L. Moreschini, D. H. Lee, A. Bostwick, C. Jozwiak, J. G. Analytis, and A. Lanzara, "Revealing the electronic structure of the current-induced metastable state in 1T-TaS₂," *Communications Physics* **8** (2025), 10.1038/s42005-025-02367-9.

¹²K. Sun, S. Sun, C. Zhu, H. Tian, H. Yang, and J. Li, "Hidden CDW states and insulator-to-metal transition after a pulsed femtosecond laser excitation in layered chalcogenide 1T-TaS_{2-x}Se_x," *Science Advances* **4** (2018), 10.1126/sciadv.aas9660.

¹³A. P. Place, L. V. Rodgers, P. Mundada, B. M. Smitham, M. Fitzpatrick, Z. Leng, A. Premkumar, J. Bryon, A. Vrajitoarea, S. Sussman, G. Cheng, T. Madhavan, H. K. Babla, X. H. Le, Y. Gang, B. Jäck, A. Gyenis, N. Yao, R. J. Cava, N. P. de Leon, and A. A. Houck, "New material platform for superconducting transmon qubits with coherence times exceeding 0.3 milliseconds," *Nature Communications* **12** (2021), 10.1038/s41467-021-22030-5.

¹⁴S. Ganjam, Y. Wang, Y. Lu, A. Banerjee, C. U. Lei, L. Krayzman, K. Kisslinger, C. Zhou, R. Li, Y. Jia, M. Liu, L. Frunzio, and R. J. Schoekopf, "Surpassing millisecond coherence in on chip superconducting quantum memories by optimizing materials and circuit design," *Nature Communications* **15** (2024), 10.1038/s41467-024-47857-6.

¹⁵M. P. Bland, F. Bahrami, J. G. Martinez, P. H. Prestegard, B. M. Smitham, A. Joshi, E. Hedrick, S. Kumar, A. Yang, A. C. Pakpour-Tabrizi, A. Jindal, R. D. Chang, G. Cheng, N. Yao, R. J. Cava, N. P. de Leon, and A. A. Houck, "Millisecond lifetimes and coherence times in 2d transmon qubits," *Nature* **647**, 343–348 (2025).

¹⁶J. S. Oh, R. Zaman, A. A. Murthy, M. Bal, F. Crisa, S. Zhu, C. G. Torres-Castore, C. J. Kopas, J. Y. Mutus, D. Jing, J. Zasadzinski, A. Grassellino, A. Romanenko, M. C. Hersam, M. J. Bedzyk, M. Kramer, B. C. Zhou, and L. Zhou, "Structure and formation mechanisms in tantalum and niobium oxides in superconducting quantum circuits," *ACS Nano* **18**, 19732–19741 (2024).

¹⁷L. N. Majer, S. Smink, W. Braun, B. Fenk, V. Harbola, B. Stuhlhofer, H. Wang, P. A. van Aken, J. Mannhart, and F. V. Hensling, "α-Ta films on c-plane sapphire with enhanced microstructure," *APL Materials* **12** (2024), 10.1063/5.0218021.

¹⁸Z. Zhang, Z. Wang, X. Dai, Y. Chen, S. Lai, F. Qin, X. Zhou, C. Wu, H. Wang, J. Yang, B. Chen, H. Zhai, Y. Zhou, M. Chen, J. Du, Z. Jiao, and M. Fang, "Bulk superconductivity in transition metal oxide TaO," *Physica C: Superconductivity and its Applications* **608** (2023), 10.1016/j.physc.2023.1354252.

¹⁹X. Cao, Z. Liu, J. Lu, W. Pan, Y. Wang, Y. Shi, S. Hong, M. Qin, G. Cao, M. Zhang, H. Tian, and Y. Xie, "Observation of superconductivity up to 8.7 k in reduced potassium tantalate," *Advanced Quantum Technologies* **7** (2024), 10.1002/qute.202400255.

²⁰M. J. Lee, C. B. Lee, D. Lee, S. R. Lee, M. Chang, J. H. Hur, Y. B. Kim, C. J. Kim, D. H. Seo, S. Seo, U. I. Chung, I. K. Yoo, and K. Kim, "A fast, high-endurance and scalable non-volatile memory device made from asymmetric Ta₂O_{5-x}/TaO_{2-x} bilayer structures," *Nature Materials* **10**, 625–630 (2011).

²¹H. Schäfer and G. Breil, "Über das system Nb₂O₅—Ta₂O₅—NbO₂—TaO₂—H₂O—H₂," *ZAAC - Journal of Inorganic and General Chemistry* **267**, 265–276 (1952).

²²N. Schönberg, "An x-ray investigation of the tantalum-oxygen system," *Acta Chemica Scandinavica* **8**, 240–245 (1954).

²³N. Terao, "Structure des oxides de tantal," *Japanese Journal of Applied Physics* **6**, 21 (1967).

²⁴Y. Syono, M. Kikuchi, T. Goto, and K. Fukuoka, "Formation of rutile-type Ta(IV)O₂ by shock reduction and cation-deficient Ta_{0.8}O₂ by subsequent oxidation," *Tech. Rep.* (1983).

²⁵Y. Muraoka, Y. Fujimoto, M. Kameoka, Y. Matsuura, M. Sunagawa, K. Terashima, T. Wakita, and T. Yokoya, "Preparation of TaO₂ thin films using NbO₂ template layers by a pulsed laser deposition technique," *Thin Solid Films* **599**, 125–132 (2016).

²⁶T. Schwaigert, S. Salmani-Rezaie, M. R. Barone, H. Paik, E. Ray, M. D. Williams, D. A. Muller, D. G. Schlom, and K. Ahadi, "Molecular beam epitaxy of KTaO₃," *Journal of Vacuum Science & Technology A* **41** (2023), 10.1116/6.0002223.

²⁷K. Fukushima, G. H. Takaoka, and I. Yamada, "Epitaxial growth of TiO₂ rutile thin films on sapphire substrates by a reactive ionized cluster beam method," *Japanese Journal of Applied Physics* **32**, 3561–3565 (1993).

²⁸S.-L. Shang, S. Lin, M. C. Gao, D. G. Schlom, and Z.-K. Liu, "Ellingham diagrams of binary oxides," *APL Materials* **12** (2024), 10.1063/5.0216426.

²⁹M. Kubovsky, Y. A. Birkhölzer, L. B. Mitrovic, H. Paik, G. R. Rossman, and D. G. Schlom, "Preparation and evaluation of new substrates for the epitaxial growth of rutile oxides," *under review* (2025).

³⁰D. C. Sun, S. Senz, and D. Hesse, "Topotaxial formation of Mg₄Ta₂O₉ and MgTa₂O₆ thin films by vapour-solid reactions on MgO (001) crystals," *Journal of the European Ceramic Society* **24**, 2453–2463 (2004).

³¹K. Azizie, F. V. Hensling, C. A. Gorsak, Y. Kim, N. A. Pieczulewski, D. M. Dryden, M. K. Senevirathna, S. Coye, S. L. Shang, J. Steele, P. Vogt, N. A. Parker, Y. A. Birkhölzer, J. P. McCandless, D. Jena, H. G. Xing, Z. K. Liu, M. D. Williams, A. J. Green, K. Chabak, D. A. Muller, A. T. Neal, S. Mou, M. O. Thompson, H. P. Nair, and D. G. Schlom, "Silicon-doped β-Ga₂O₃ films grown at 1 μm/h by suboxide molecular-beam epitaxy," *APL Materials* **11** (2023), 10.1063/5.0139622.

³²<https://ipcol.com/cleaners/micro-90>.

³³S. J. Schneider, "Cooperative determination of the melting point of alumina," *Pure and Applied Chemistry* **21**, 115–122 (1970).

³⁴R. M. Sova, M. J. Linevsky, M. E. Thomas, and F. F. Mark, "High-temperature infrared properties of sapphire, alon, fused silica, yttria, and spinel," *Infrared Physics & Technology* **39**, 251–261 (1998).

³⁵W. Braun and J. Mannhart, "Film deposition by thermal laser evaporation," *AIP Advances* **9** (2019), 10.1063/1.5111678.

³⁶T. J. Smart, J. Mannhart, and W. Braun, "Thermal laser evaporation of elements from across the periodic table," *Journal of Laser Applications* **33** (2021), 10.2351/7.0000348.

³⁷F. V. Hensling, W. Braun, D. Y. Kim, L. N. Majer, S. Smink, B. D. Faeth, and J. Mannhart, "State of the art, trends, and opportunities for oxide epitaxy," *APL Materials* **12** (2024), 10.1063/5.0196883.

³⁸N. Wadehra, B. Z. Gregory, S. Zhang, N. Schnitzer, Y. Iguchi, Y. E. Li, B. Pamuk, D. A. Muller, A. Singer, K. M. Shen, and D. G. Schlom, "Strain-induced superconductivity in RuO₂ (100) thin-films," *Communications Materials* **6** (2025), 10.1038/s43246-025-00856-6.

³⁹B. H. Savitzky, I. E. Baggari, C. B. Clement, E. Waite, B. H. Goodge, D. J. Baek, J. P. Sheckelton, C. Pasco, H. Nair, N. J. Schreiber, J. Hoffman, A. S. Admasu, J. Kim, S. W. Cheong, A. Bhattacharya, D. G. Schlom, T. M. McQueen, R. Hovden, and L. F. Kourkoutis, "Image registration of low signal-to-noise cryo-STEM data," *Ultramicroscopy* **191**, 56–65 (2018).

⁴⁰H. T. Philipp, M. W. Tate, K. S. Shanks, L. Mele, M. Peemen, P. Dona, R. Hartong, G. V. Veen, Y. T. Shao, Z. Chen, J. Thom-Levy, D. A. Muller, and S. M. Gruner, "Very-high dynamic range, 10,000 frames/second pixel array detector for electron microscopy," *Microscopy and Microanalysis* **28**,

425–440 (2022).

⁴¹P. Thibault and A. Menzel, “Reconstructing state mixtures from diffraction measurements,” *Nature* **494**, 68–71 (2013).

⁴²K. Wakanig, H. C. Stadler, M. Odstrcil, E. H. Tsai, A. Diaz, M. Holler, I. Usov, J. Raabe, A. Menzel, and M. Guizar-Sicairos, “Ptychoshelves, a versatile high-level framework for high-performance analysis of ptychographic data,” *Journal of Applied Crystallography* **53**, 574–586 (2020).

⁴³Z. Chen, Y. Jiang, Y.-T. Shao, M. E. Holtz, M. Odstrcil, M. Guizar-Sicairos, I. Hanke, S. Ganschow, D. G. Schlom, and D. A. Muller, “Electron ptychography achieves atomic-resolution limits set by lattice vibrations,” *Tech. Rep.* (2021).

⁴⁴Z. Chen, M. Odstrcil, Y. Jiang, Y. Han, M. H. Chiu, L. J. Li, and D. A. Muller, “Mixed-state electron ptychography enables sub-angstrom resolution imaging with picometer precision at low dose,” *Nature Communications* **11** (2020), 10.1038/s41467-020-16688-6.

⁴⁵C. Zhang, Y.-T. Shao, Z. Baraissov, C. J. Duncan, A. Hanuka, A. L. Edelen, J. M. Maxson, and D. A. Muller, “Bayesian optimization for multi-dimensional alignment: Tuning aberration correctors and ptychographic reconstructions,” *Microscopy and Microanalysis* **28**, 3146–3148 (2022).

⁴⁶I. C. G. van den Bosch, J. U. Zaman, G. Shterk, M. H. Hamed, M. Schneider, V. Ratovskii, Y. Bu, P. M. Dietrich, G. Koster, and C. Baeumer, “Laboratory-based *in situ* and *operando* tricolor x-ray photoelectron spectroscopy,” *Science Advances* **11** (2025), 10.1126/sciadv.adw6673.

⁴⁷D. C. Grinter, P. Ferrer, F. Venturini, M. A. van Spronken, A. I. Large, S. Kumar, M. Jaugstetter, A. Iordachescu, A. Watts, S. L. M. Schroeder, A. Kroner, F. Grillo, S. M. Francis, P. B. Webb, M. Hand, A. Walters, M. Hillman, and G. Held, “VerSoX B07-B: a high-throughput XPS and ambient pressure NEXAFS beamline at Diamond Light Source,” *Journal of Synchrotron Radiation* **31**, 578–589 (2024).

⁴⁸J. N. Hilfiker, C. L. Bungay, R. A. Synowicki, T. E. Tiwald, C. M. Herzinger, B. Johs, G. K. Pribil, and J. A. Woollam, “Progress in spectroscopic ellipsometry: Applications from vacuum ultraviolet to infrared,” *Journal of Vacuum Science & Technology A: Vacuum, Surfaces, and Films* **21**, 1103–1108 (2003).

⁴⁹B. Johs, J. A. Woollam, C. M. Herzinger, J. N. Hilfiker, R. A. Synowicki, and C. L. Bungay, “Overview of variable-angle spectroscopic ellipsometry (vase): II. advanced applications,” (1999) pp. 55–87.

⁵⁰J. A. Woollam, B. D. Johs, C. M. Herzinger, J. N. Hilfiker, R. A. Synowicki, and C. L. Bungay, “Overview of variable-angle spectroscopic ellipsometry (vase): I. basic theory and typical applications,” (1999) pp. 3–28.

⁵¹Y. A. Birkhölzer, K. Sotthewes, N. Gauquelin, L. Riekehr, D. Jannis, E. van der Minne, Y. Bu, J. Verbeeck, H. J. W. Zandvliet, G. Koster, and G. Rijnders, “High-strain-induced local modification of the electronic properties of VO₂ thin films,” *ACS Applied Electronic Materials* **4**, 6020–6028 (2022).

⁵²N. F. Quackenbush, H. Paik, J. C. Woicik, D. A. Arena, D. G. Schlom, and L. F. Piper, “X-ray spectroscopy of ultra-thin oxide/oxide heteroepitaxial films: A case study of single-nanometer VO₂/TiO₂,” *Materials* **8**, 5452–5466 (2015).

⁵³G. J. P. Fajardo, S. A. Howard, E. Evlyukhin, M. J. Wahila, W. R. Mondal, M. Zuba, J. E. Boschker, H. Paik, D. G. Schlom, J. T. Sadowski, S. A. Tenney, B. Reinhart, W. C. Lee, and L. F. Piper, “Structural phase transitions of NbO₂: Bulk versus surface,” *Chemistry of Materials* **33**, 1416–1425 (2021).

⁵⁴D. Zheng, C. N. Young, and W. F. Stickle, “HAXPES reference spectra of Ta and Ta₂O₅ with Cr K α excitation,” *Surface Science Spectra* **30** (2023), 10.1116/6.0002551.

⁵⁵While the temperature and pressure at which oxidation was observed in *operando* HAXPES was nominally comparable to the MBE growth conditions, calibration differences between different chambers and laboratories likely exist.

⁵⁶L. J. Ament, M. V. Veenendaal, T. P. Devereaux, J. P. Hill, and J. V. D. Brink, “Resonant inelastic x-ray scattering studies of elementary excitations,” *Reviews of Modern Physics* **83**, 705–767 (2011).

⁵⁷H. Ishikawa, T. Takayama, R. K. Kremer, J. Nuss, R. Dinnebier, K. Kitagawa, K. Ishii, and H. Takagi, “Ordering of hidden multipoles in spin-orbit entangled 5d¹ ta chlorides,” *Physical Review B* **100** (2019), 10.1103/PhysRevB.100.045142.

⁵⁸A. Revelli, M. M. Sala, G. Monaco, P. Becker, L. Bohatý, M. Hermanns, T. C. Koethe, T. Fröhlich, P. Warzanowski, T. Lorenz, S. V. Streltsov, P. H. M. van Loosdrecht, D. I. Khomskii, J. van den Brink, and M. Grüninger, “Resonant inelastic x-ray incarnation of young’s double-slit experiment,” *Science Advances* **5** (2019), 10.1126/sciadv.aav4020.

⁵⁹M. Magnaterra, J. Attig, L. Peterlini, M. Hermanns, M. H. Upton, J. Kim, L. Prodan, V. Tsurkan, I. Kézsmárki, P. H. V. Loosdrecht, and M. Grüninger, “Quasimolecular $j_{\text{tot}} = 3/2$ moments in the cluster mott insulator GaTa₄Se₈,” *Physical Review Letters* **133** (2024), 10.1103/PhysRevLett.133.046501.

⁶⁰J. H. Oh, J. H. Kim, J. H. Jeong, and S. H. Chang, “Resonant inelastic x-ray scattering of tantalum double perovskite structures,” *Current Applied Physics* **18**, 1225–1229 (2018).

⁶¹A. Gössling, R. Schmitz, H. Roth, M. W. Haverkort, T. Lorenz, J. A. Mydosh, E. Müller-Hartmann, and M. Grüninger, “Mott-hubbard exciton in the optical conductivity of YTiO₃ and SmTiO₃,” *Physical Review B - Condensed Matter and Materials Physics* **78** (2008), 10.1103/PhysRevB.78.075122.

⁶²J. Reul, A. A. Nugroho, T. T. Palstra, and M. Grüninger, “Probing orbital fluctuations in RVO₃ (R = Y, Gd, or Ce) by ellipsometry,” *Physical Review B - Condensed Matter and Materials Physics* **86** (2012), 10.1103/PhysRevB.86.125128.

⁶³I. Vergara, M. Magnaterra, P. Warzanowski, J. Attig, S. Kunkemöller, D. I. Khomskii, M. Braden, M. Hermanns, and M. Grüninger, “Spin-orbit coupling and crystal-field splitting in ti-doped Ca₂RuO₄ studied by ellipsometry,” *Physical Review B* **106** (2022), 10.1103/PhysRevB.106.085103.

⁶⁴S. J. Moon, H. Jin, W. S. Choi, J. S. Lee, S. S. Seo, J. Yu, G. Cao, T. W. Noh, and Y. S. Lee, “Temperature dependence of the electronic structure of the $j_{\text{eff}} = 1/2$ mott insulator Sr₂IrO₄ studied by optical spectroscopy,” *Physical Review B - Condensed Matter and Materials Physics* **80** (2009), 10.1103/PhysRevB.80.195110.

⁶⁵V. Guiot, L. Cario, E. Janod, B. Corraze, V. T. Phuoc, M. Rozenberg, P. Stoliar, T. Cren, and D. Roditchev, “Avalanche breakdown in GaTa₄Se_{8-x}Te_x narrow-gap Mott insulators,” *Nature Communications* **4** (2013), 10.1038/ncomms2735.

⁶⁶J. H. Hur, “First principles study of the strain effect on band gap of λ phase Ta₂O₅,” *Computational Materials Science* **164**, 17–21 (2019).

⁶⁷M. Prato, A. Chincarini, G. Gemme, and M. Canepa, “Gravitational waves detector mirrors: Spectroscopic ellipsometry study of Ta₂O₅ films on SiO₂ substrates,” *Thin Solid Films* **519**, 2877–2880 (2011).

⁶⁸Other ions with a comparable ionic radius to Ta⁴⁺ are Li¹⁺ and Sc³⁺ as well as W⁵⁺ and Re⁵⁺.

⁶⁹C. B. Alcock, V. P. Itkin, and M. K. Horrigan, “Vapour pressure equations for the metallic elements: 298–2500 k,” *Canadian Metallurgical Quarterly* **23**, 309–313 (1984).

⁷⁰K. M. Adkison, S. L. Shang, B. J. Bocklund, D. Klimm, D. G. Schlom, and Z. K. Liu, “Suitability of binary oxides for molecular-beam epitaxy source materials: A comprehensive thermodynamic analysis,” *APL Materials* **8** (2020), 10.1063/5.0013159.

⁷¹L. B. Freund and S. Suresh, *Thin Film Materials : Stress, Defect Formation and Surface Evolution* (Cambridge University Press, 2004) p. 32.

⁷²D. A. Shirley, “High-resolution x-ray photoemission spectrum of the valence bands of gold,” *Physical Review B* **5**, 4709–4714 (1972).

⁷³P. Hohenberg and W. Kohn, “Inhomogeneous electron gas,” *Physical Review* **136**, B864–B871 (1964).

⁷⁴W. Kohn and L. J. Sham, “Self-consistent equations including exchange and correlation effects,” *Physical Review* **140**, A1133–A1138 (1965).

⁷⁵F. Karsai, M. Humer, E. Flage-Larsen, P. Blaha, and G. Kresse, “Effects of electron-phonon coupling on absorption spectrum: K edge of hexagonal boron nitride,” *Physical Review B* **98**, 235205 (2018).

⁷⁶G. Kresse and J. Furthmüller, “Efficient iterative schemes for ab initio total-energy calculations using a plane-wave basis set,” *Physical Review B* **54**, 11169–11186 (1996).

⁷⁷P. E. Blöchl, “Projector augmented-wave method,” *Physical Review B* **50**, 17953–17979 (1994).

⁷⁸D. M. Ceperley and B. J. Alder, “Ground state of the electron gas by a stochastic method,” *Physical Review Letters* **45**, 566–569 (1980).

⁷⁹J. P. Perdew and A. Zunger, “Self-interaction correction to density-functional approximations for many-electron systems,” *Physical Review B* **23**, 5048–5079 (1981).

⁸⁰E. Amonette, P. Dulal, D. Sotir, M. Barone, D. Schlom, and N. J. Podraza, “Band gap energy and near infrared to ultraviolet complex optical

properties of single crystal TbScO₃,” *Applied Physics Letters* **123** (2023), 10.1063/5.0146670.

⁸¹G. E. Jellison, N. J. Podraza, and A. Shan, “Ellipsometry: dielectric functions of anisotropic crystals and symmetry,” *Journal of the Optical Society of America A* **39**, 2225 (2022).

⁸²B. Johs and C. M. Herzinger, “Quantifying the accuracy of ellipsometer systems,” *physica status solidi c* **5**, 1031–1035 (2008).

⁸³D. Aspnes, “Optical properties of thin films,” *Thin Solid Films* **89**, 249–262 (1982).

⁸⁴D. Schmidt and M. Schubert, “Anisotropic Bruggeman effective medium approaches for slanted columnar thin films,” *Journal of Applied Physics* **114** (2013), 10.1063/1.4819240.

⁸⁵H. Yao and C. H. Yan, “Anisotropic optical responses of sapphire (α -Al₂O₃) single crystals,” *Journal of Applied Physics* **85**, 6717–6722 (1999).

⁸⁶H. G. Tompkins and E. A. Irene, *Handbook of ellipsometry* (William Andrew Pub. ; Springer, 2005) p. 870.

⁸⁷A. K. Harman, S. Ninomiya, and S. Adachi, “Optical constants of sapphire (α -Al₂O₃) single crystals,” *Journal of Applied Physics* **76**, 8032–8036 (1994).

⁸⁸W. J. Tropf and M. E. Thomas, “Aluminum oxide (Al₂O₃) revisited,” in *Handbook of Optical Constants of Solids* (Elsevier, 1997) pp. 653–682.

⁸⁹M. A. Jeppesen, “Some optical, thermo-optical, and piezo-optical properties of synthetic sapphire,” *Journal of the Optical Society of America* **48**, 629 (1958).

⁹⁰L. K. Gautam, H. Haneef, M. Junda, D. S. John, and N. Podraza, “Approach for extracting complex dielectric function spectra in weakly-absorbing regions,” *Thin Solid Films* **571**, 548–553 (2014).

⁹¹D. Adhikari, M. M. Junda, P. Uperty, K. Ghimire, I. Subedi, and N. J. Podraza, “Near infrared to ultraviolet anisotropic optical properties of single crystal SrLaAlO₄ from spectroscopic ellipsometry,” *physica status solidi (b)* **253**, 2066–2072 (2016).

⁹²K. Ghimire, H. F. Haneef, R. W. Collins, and N. J. Podraza, “Optical properties of single-crystal Gd₃Ga₅O₁₂ from the infrared to ultraviolet,” *physica status solidi (b)* **252**, 2191–2198 (2015).

⁹³M. Barone, M. Foody, Y. Hu, J. Sun, B. Frye, S. S. Perera, B. Subedi, H. Paik, J. Hollin, M. Jeong, K. Lee, C. H. Winter, N. J. Podraza, K. Cho, A. Hock, and D. G. Schlom, “Growth of Ta₂SnO₆ films, a candidate wide-band-gap p-type oxide,” *The Journal of Physical Chemistry C* **126**, 3764–3775 (2022).

⁹⁴W. Oldham, “Numerical techniques for the analysis of lossy films,” *Surface Science* **16**, 97–103 (1969).

⁹⁵G. E. Jellison and F. A. Modine, “Parameterization of the optical functions of amorphous materials in the interband region,” *Applied Physics Letters* **69**, 371–373 (1996).

⁹⁶J. I. Pankove, *Optical processes in semiconductors* (Dover Publications, 1975) p. 422.

⁹⁷G. Kresse and J. Hafner, “*Ab initio* molecular dynamics for liquid metals,” *Phys. Rev. B* **47**, 558–561 (1993).

⁹⁸G. Kresse and J. Furthmüller, “Efficiency of ab-initio total energy calculations for metals and semiconductors using a plane-wave basis set,” *Computational Materials Science* **6**, 15–50 (1996).

⁹⁹G. Kresse and J. Furthmüller, “Efficient iterative schemes for *ab initio* total-energy calculations using a plane-wave basis set,” *Phys. Rev. B* **54**, 11169–11186 (1996).

¹⁰⁰G. Kresse and D. Joubert, “From ultrasoft pseudopotentials to the projector augmented-wave method,” *Phys. Rev. B* **59**, 1758–1775 (1999).

¹⁰¹L. Zhu, J. Zhou, Z. Guo, and Z. Sun, “Realization of a reversible switching in TaO₂ polymorphs via Peierls distortion for resistance random access memory,” *Applied Physics Letters* **106**, 091903 (2015).

¹⁰²S. L. Dudarev, G. A. Botton, S. Y. Savrasov, C. J. Humphreys, and A. P. Sutton, “Electron-energy-loss spectra and the structural stability of nickel oxide: An LSDA+U study,” *Phys. Rev. B* **57**, 1505–1509 (1998).

¹⁰³M. Cococcioni and S. de Gironcoli, “Linear response approach to the calculation of the effective interaction parameters in the LDA + U method,” *Phys. Rev. B* **71**, 035105 (2005).

¹⁰⁴M. Gajdoš, K. Hummer, G. Kresse, J. Furthmüller, and F. Bechstedt, “Linear optical properties in the projector-augmented wave methodology,” *Phys. Rev. B* **73**, 045112 (2006).

¹⁰⁵D. Sangalli, J. A. Berger, C. Attaccalite, M. Grüning, and P. Romaniello, “Optical properties of periodic systems within the current-current response framework: Pitfalls and remedies,” *Phys. Rev. B* **95**, 155203 (2017).

¹⁰⁶H. T. Stokes, D. M. Hatch, and B. J. Campbell, “ISOTROPY Software Suite,” Iso.byu.edu.

¹⁰⁷H. T. Stokes, S. van Orden, and B. J. Campbell, “ISOSUBGROUP: an internet tool for generating isotropy subgroups of crystallographic space groups,” *Journal of Applied Crystallography* **49**, 1849–1853 (2016).

¹⁰⁸T. Birol, *An Ab Initio Study Of The Structural, Magnetic, And Electronic Properties Of Transition Metal Oxides*, Phd thesis, Cornell University, Ithaca, NY (2013), <https://ecommons.cornell.edu/items/3168dac7-f793-481d-9fe0-feddf2aacb39>.

Supporting Information

S1. SUBOXIDE MOLECULAR-BEAM EPITAXY

A. Vapor pressure

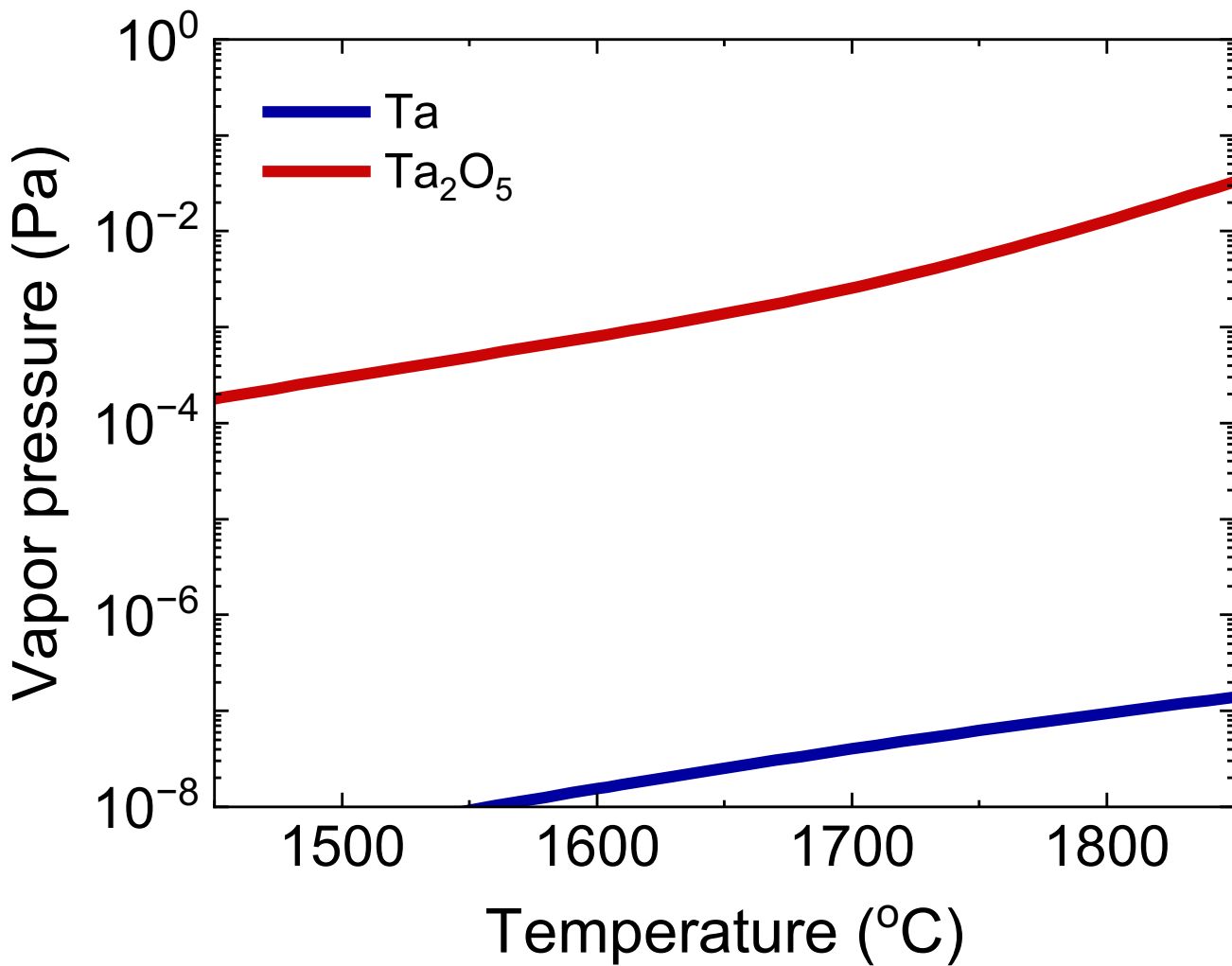


FIG. S1. Vapor pressure of tantalum over tantalum metal (blue) and total vapor pressure of species emanating from a Ta_2O_5 charge (red) as a function of temperature. The tantalum vapor pressure was computed based on an equation published by Alcock, Itkin, and Horrigan⁶⁹; the Ta_2O_5 vapor pressure data were previously published by Adkison *et al.*⁷⁰.

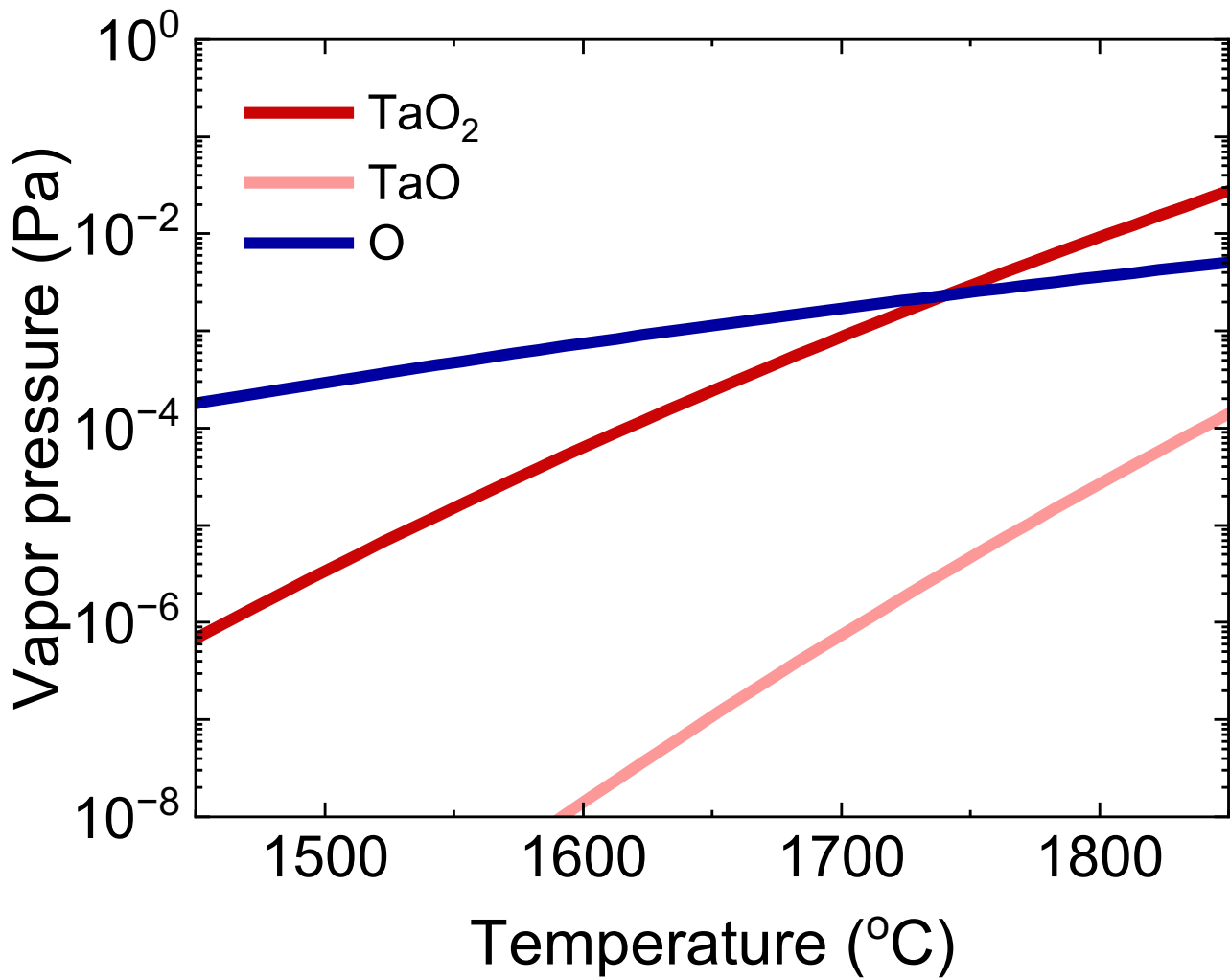


FIG. S2. Partial vapor pressure of species emanating from a Ta_2O_5 charge as a function of temperature showing the dominance of $\text{TaO}_2 \gtrsim 1740^{\circ}\text{C}$. The same data were previously published by Adkison *et al.*⁷⁰.

S2. EPITAXIAL RELATIONSHIP BETWEEN RUTILE AND *r*-PLANE SAPPHIRE

As the only two commercially available rutile substrates TiO₂ and MgF₂ are not stable under the high temperatures (around 1000 °C) and reducing conditions (below 1×10^{-8} Torr) necessary to crystallize TaO₂, we had to search for alternative substrates that may enable heteroepitaxial growth of rutile. We selected *r*-plane sapphire, which shows a similar surface motif to rutile (101).

As the cross-sectional schematics in Fig. 1 illustrate, the heteroepitaxial interface between Al₂O₃ (1 $\bar{1}$ 02) and TaO₂ (101) is highly anisotropic. While the lattice mismatch in one direction is very small (see Fig. 1 (a)) resulting in a commensurately strained epitaxial film, the mismatch is so big in the orthogonal direction (see Fig. 1 (b)) that it leads to periodic defects. The commensurate in-plane direction is TaO₂ [010] (b_{rutile}), which is parallel to Al₂O₃ [11 $\bar{2}$ 0]. The incommensurate in-plane direction is TaO₂ [$\bar{1}$ 01], which is parallel to Al₂O₃ [$\bar{1}$ 101]. The misfit strains⁷¹ in the two directions are:

$$\varepsilon = \frac{a_{\text{substrate}} - a_{\text{film}}}{a_{\text{film}}}$$

$$\varepsilon_{\text{com}} = \frac{4.762 - 4.752}{4.752} \approx 0.2\%$$

$$\varepsilon_{\text{incom}} = \frac{5.130 - 5.667}{5.667} \approx -9.5\%$$

where a_{film} is the stress-free lattice parameter of the film material and $a_{\text{substrate}}$ is the lattice parameter of the substrate. For TaO₂, we use the values published by Syono *et al.*²⁴ (PDF number 01-079-9603).

The experimental data confirming this anisotropic strain states are shown in Figs. 4, 5 and S7. A schematic top-view of the interfacial alignment of TaO₂ (101) on Al₂O₃ (1 $\bar{1}$ 02) is shown in Fig. S3.

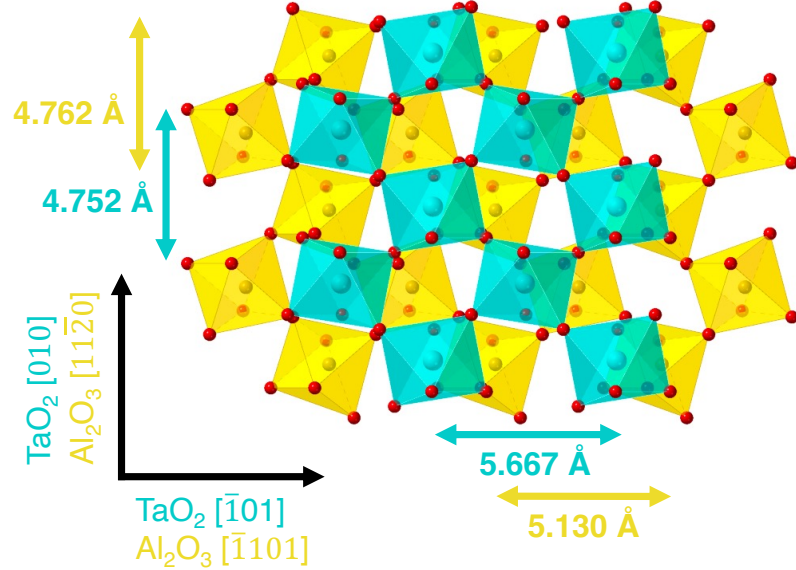


FIG. S3. Schematic top view of TaO₂ (101) on Al₂O₃ (1 $\bar{1}$ 02). For clarity, only one monolayer of the substrate and the film are depicted. The indicated lattice parameters are unstrained bulk values.

S3. ATOMIC FORCE MICROSCOPY

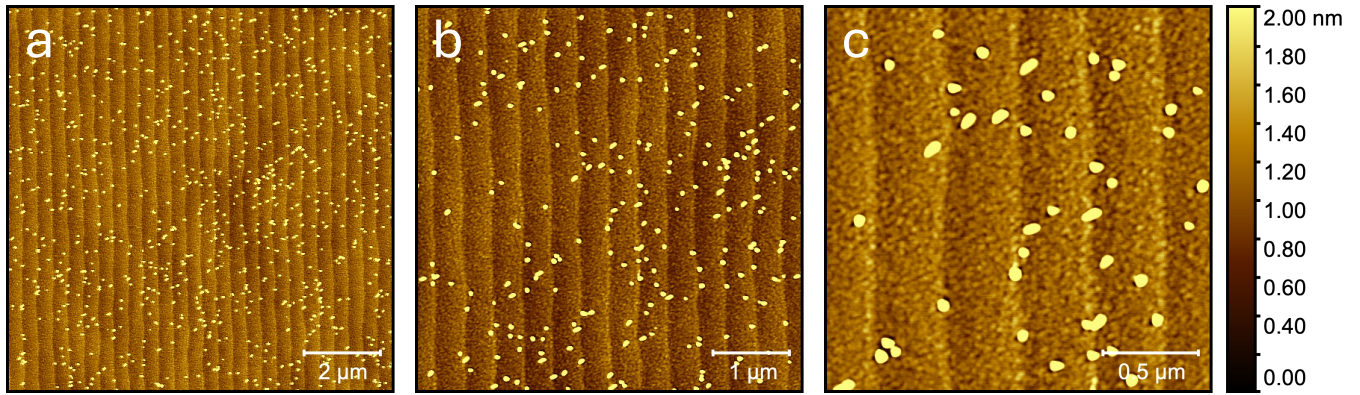


FIG. S4. AFM of MBE-grown TaO_2 (101) on Al_2O_3 (1-102). Field of view 10x10 (a), 5x5 (b), and 2x2 μm^2 (c).

AFM topography images reveal that the step-and-terrace structure of the underlying Al_2O_3 (1-102) substrate is preserved during TaO_2 film growth by *S*-MBE. The nominal thickness of the TaO_2 film is 11.4 nm. The surface appears smooth, except for a few nanometer-sized particles.

S4. X-RAY DIFFRACTION PHI SCANS

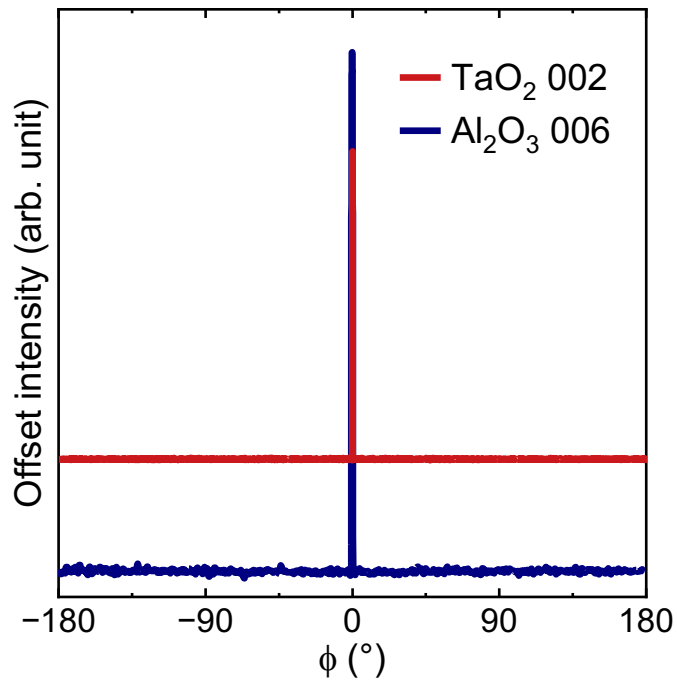


FIG. S5. XRD ϕ -scans of MBE-grown TaO_2 (101) on Al_2O_3 ($1\bar{1}02$) confirming the untwinned nature of the film. The rutile and corundum c -axes point in the same in-plane direction.

S5. RHEED

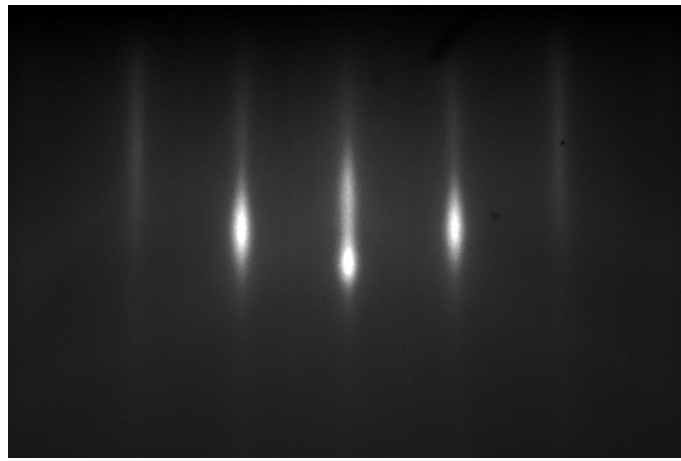


FIG. S6. Reflective high-energy electron diffraction (RHEED) image of MBE-grown TaO_2 taken at room temperature along the [010] direction of the film.

S6. RECIPROCAL SPACE MAPS

To verify the long-range order and orientational alignment inferred from STEM imaging and laboratory-source XRD measurement, we performed additional synchrotron X-ray measurements, mapping a wide range of three-dimensional reciprocal space. Figure S7 shows two orthogonal slices of the 3D dataset. Panels (a, b) depict a $K - L$ plot at $H = 1$ (index referring to the rutile TaO₂ film), panels (c, d) depict a $H - L$ plot at $K = 1$. To aid navigation in these feature-rich plots, we performed single crystal diffraction simulations using the program SingleCrystal (version 5.1.1) by CrystalMaker Software Ltd.

The fact that the simulations can uniquely index every experimentally observed peak proves the untwinned nature of the TaO₂ film. The reason for this is the unique epitaxial match between rutile and *r*-plane sapphire, which lacks rotational symmetry at the interface that would lead to twinning.

For panels (a, b) in Fig. S7, the view direction is parallel to the TaO₂ lattice vector $[\bar{1}01]$ while the vertical direction is normal to the (101) plane. The substrate view direction is parallel to the Al₂O₃ lattice vector $[1\bar{1}0\bar{1}]$ while the vertical direction is normal to the (1102) plane.

For panels (c, d) in Fig. S7, the view direction is parallel to the TaO₂ lattice vector $[0\bar{1}0]$ while the vertical direction is normal to the (101) plane. The substrate view direction is parallel to the Al₂O₃ lattice vector $[11\bar{2}0]$ while the vertical direction is normal to the (1102) plane.

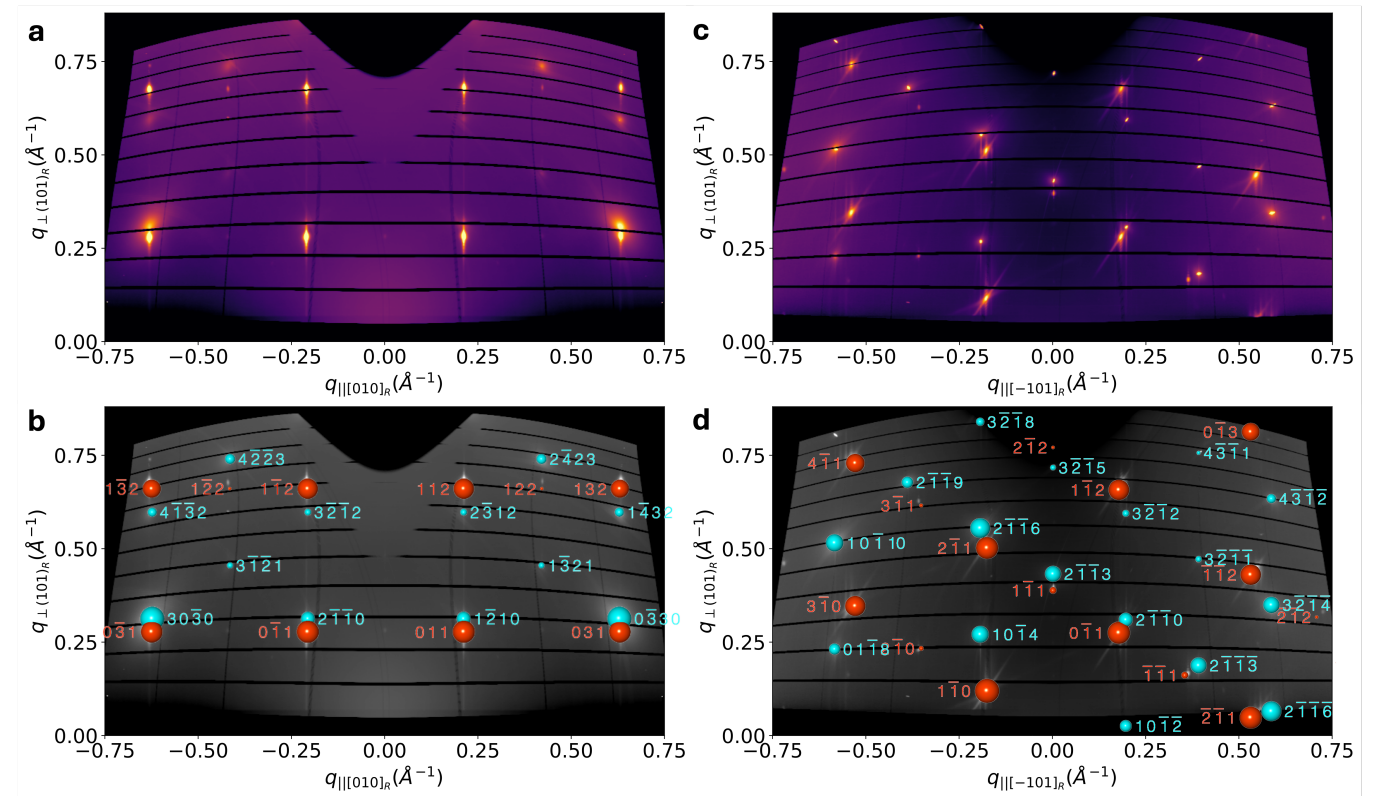


FIG. S7. Synchrotron X-ray reciprocal space maps on a false-color scale (a, c) and grayscale (b, d). Lower panels show superimposed single-crystal diffraction simulations. TaO₂ peaks are depicted and labeled in red, Al₂O₃ peaks in cyan.

S7. HIGH-TEMPERATURE X-RAY DIFFRACTION

To test the stability of TaO₂ in air at elevated temperatures, we performed *operando* XRD measurements using a temperature-controlled hot stage. The results are summarized in Fig. S8. The data shows that above 300 °C, TaO₂ oxidizes to Ta₂O₅. This reaction is irreversible and the sample remains Ta₂O₅ upon subsequent cooling.

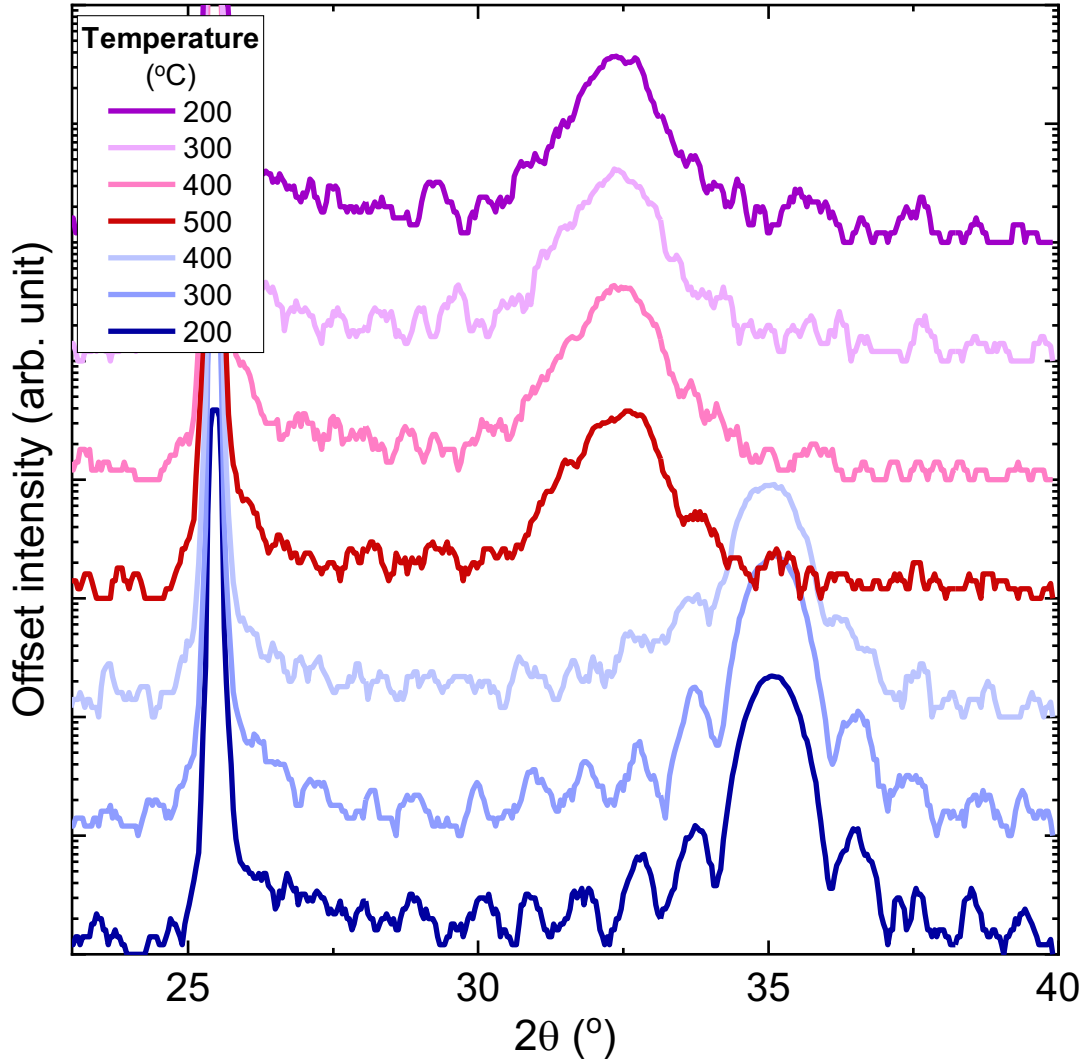


FIG. S8. XRD at elevated temperature shows the irreversible oxidation of TaO₂ to Ta₂O₅ in air above 400 °C. From bottom to top, the figure shows scans during heating and subsequent cooling measured with a Rigaku SmartLab diffractometer equipped with an Anton Paar DHS 1100 domed hot stage and a monochromated copper anode.

S8. HAXPES

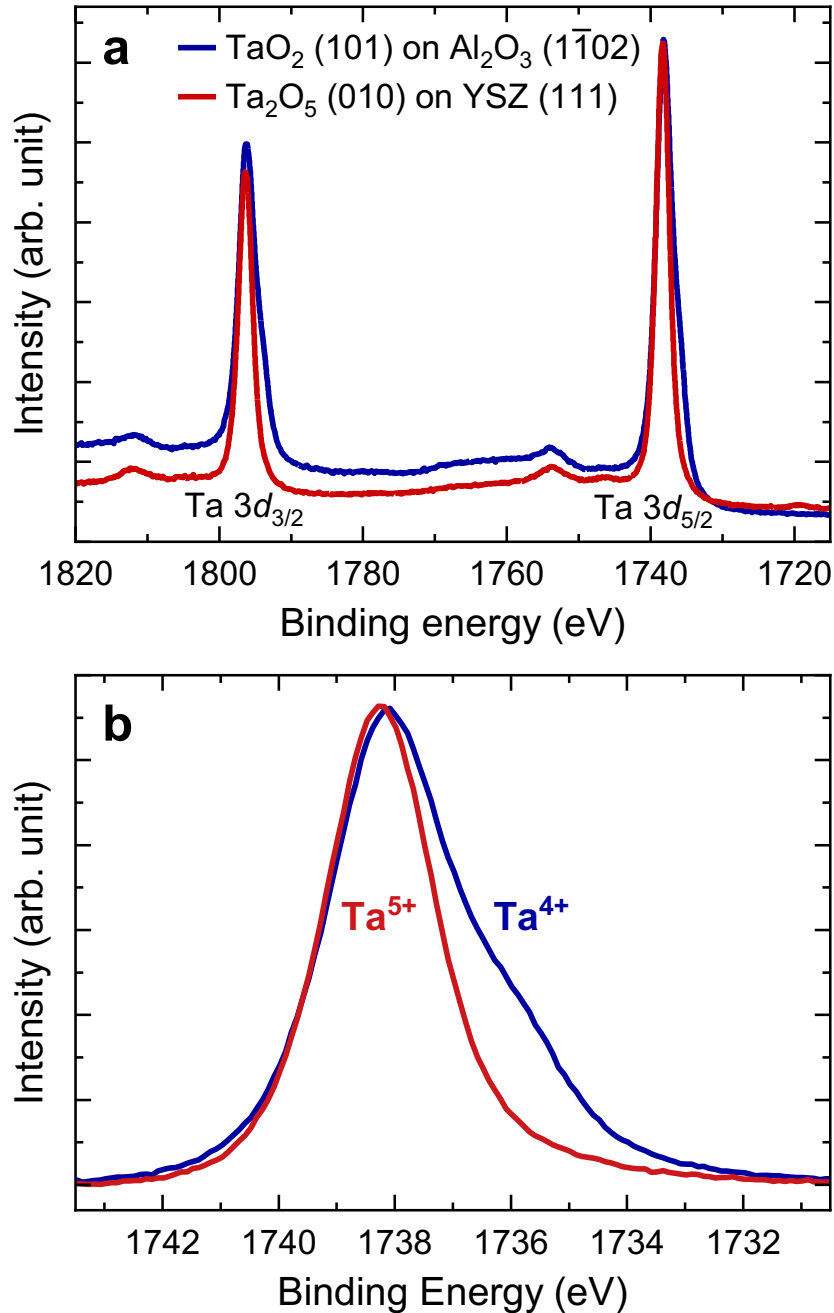


FIG. S9. Tantalum 3d HAXPES data collected using a Scienta Omicron system with a monochromated gallium liquid metal jet source operating at 9.25 keV. The TaO_2 data shows asymmetric peaks originating from the pentavalent surface layer with shoulders on the low binding energy side which we assign to the tetravalent interior of the film. The Ta_2O_5 thin film was fabricated via suboxide MBE while applying a flux of ozone gas. Both samples were exposed to air for several months prior to the measurements explaining the strong Ta^{5+} signal of the TaO_2 sample despite the increased information depth of HAXPES compared to soft X-ray photoelectron spectroscopy. Panel (b) shows a magnification of the tantalum 3d_{5/2} region after Shirley-background⁷² subtraction.

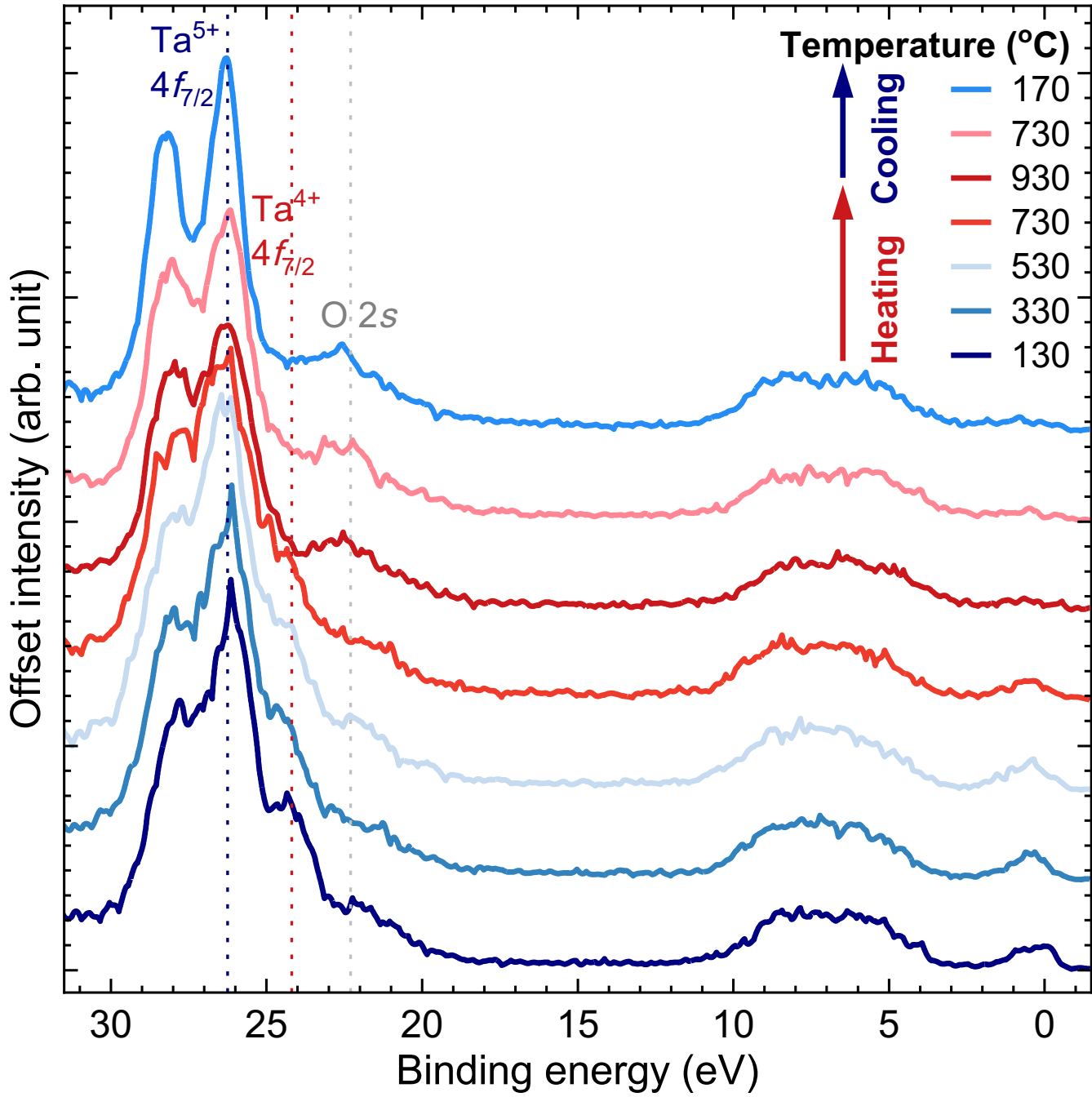


FIG. S10. Variable-temperature *operando* HAXPES. Tantalum 4f, oxygen 2s and valence band data collected using a SPECS system operating at 5.4 keV using a chromium anode. The sample was first heated and then cooled as spectra were measured. Dashed vertical lines are guides to the eye. Around 930 °C, TaO₂ irreversibly oxidized to Ta₂O₅ in UHV conditions. Residual gas analysis indicated $p\text{H}_2\text{O}$ and $p\text{O}_2 < 1 \times 10^{-8}$ Torr. The sample was exposed to air for several months prior to the measurements. Even at room temperature, the sample showed a strong Ta⁵⁺ contribution due to the surface oxidation of TaO₂.

S9. OXYGEN K-EDGE EELS

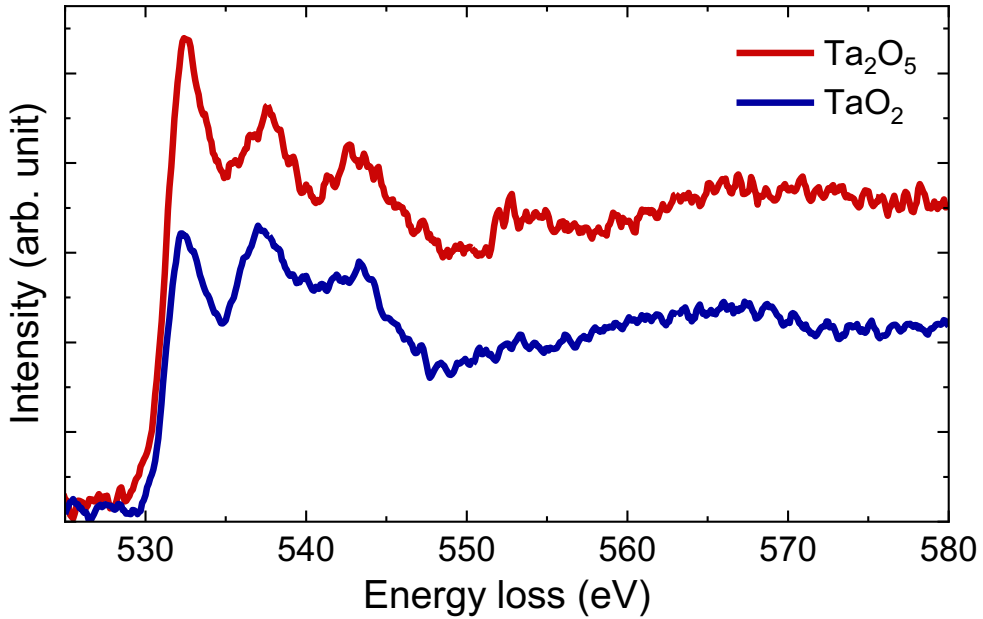


FIG. S11. Oxygen *K*-edge electron energy-loss spectroscopy comparing TaO₂ and Ta₂O₅. The key difference is the intensity of the first peak, commonly ascribed to be indicative of the t_{2g} of the metal *d*-band filling.

S10. OXYGEN K-EDGE SIMULATION

X-ray absorption spectroscopy (XAS) simulations were carried out using density-functional theory (DFT)^{73,74} within the supercell core-hole approach,⁷⁵ as implemented in the Vienna ab initio simulation package (VASP)⁷⁶ with projector-augmented wave (PAW) pseudopotentials.⁷⁷ Supercells of TaO₂ (Ta₇₂O₁₄₄) and Ta₂O₅ (Ta₇₂O₁₈₀) were used in all calculations. Approximately 4000 bands were included in the core-hole calculations. A plane-wave energy cutoff of 400 eV was employed, and the Brillouin zone was sampled using a *k*-point grid with a density of 6000 divided by the number of atoms in the supercell. The XAS spectra were obtained from the imaginary part of the frequency-dependent dielectric function. To account for instrumental resolution and core-hole lifetime effects, the calculated spectra were convoluted with a Gaussian function with a full width at half maximum (FWHM) of 0.3 eV and a Lorentzian function with a linearly increasing width from 0.0 to 0.7 eV. Several exchange–correlation functionals were tested; results presented here were obtained using the local density approximation (LDA)^{78,79} with spin polarization.

Figure S12 (a) shows a comparison of simulated XAS (or EELS) spectra for TaO₂ (in blue) and Ta₂O₅ (in red). The key difference in the simulations – as for the experimental data shown in Fig. S11 – is the ratio of the first peak (around 532 eV) compared to the second peak (around 537 eV). Fig. S12 (b) shows a comparison of the experimental EELS data of a TaO₂ lamella with a linear combination of TaO₂ and Ta₂O₅ simulations. The latter combination was simulated to mimic the oxidation of TaO₂ in air. While the ratio of TaO₂ and Ta₂O₅ was chosen to match the ratio of the first two peaks, the remainder of the O *K*-edge spectrum was not optimized.

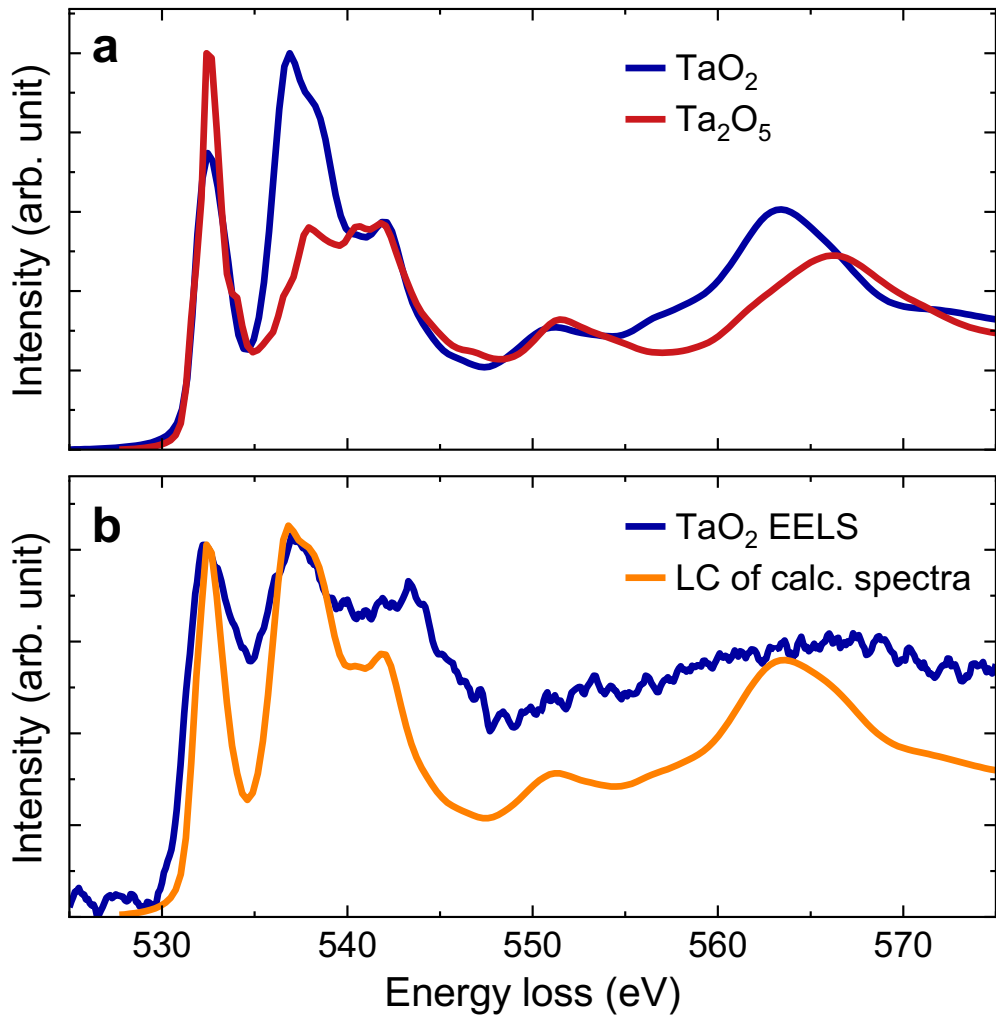


FIG. S12. Calculated oxygen K -edge electron energy-loss spectra for TaO_2 and Ta_2O_5 (a), comparison of experimental EELS data (as shown in Fig. S11) with a linear combination (LC) of calculated spectra. The LC consists of 75 % TaO_2 and 25 % Ta_2O_5 to mimic the unpreventable surface oxidation of TaO_2 .

S11. SPECTROSCOPIC ELLIPSOMETRY

A. *r*-plane Al₂O₃ substrate

For the generalized ellipsometric spectra collected for the *r*-plane Al₂O₃ substrate, all four ϕ rotations are analyzed simultaneously^{80,81} to determine surface layer thickness and Al₂O₃ complex optical properties by fitting a structural and optical model to experimental ellipsometric spectra with an iterative least square regression to minimize the mean square error (MSE).⁸² The structural model for the Al₂O₃ substrate consists of a semi-infinite single crystal substrate / surface layer / air ambient with the optical response of the surface layer described by an anisotropic Bruggeman effective medium approximation (EMA)^{83,84} consisting of equal parts Al₂O₃ and void, resulting in a surface layer thickness of 1.80 ± 0.03 nm. The polar Euler angle (θ) is fixed to 57.6° which is the angle the *c*-axis relative to the *r*-plane surface. The sample has been rotated by nominally 45° increments with the azimuthal Euler angle ϕ . The parametric model to describe the optical response of Al₂O₃ in both the ordinary and extraordinary directions consists of the parameterization developed by Yao and Yan⁸⁵ with the addition of a Sellmeier⁸⁶ expression for both the ordinary and extra ordinary directions to account for contributions from phonon modes at photon energies below the measured spectral range.⁸⁷ The anisotropic Bruggeman EMA utilizes the same directionally dependent complex optical properties and Euler angles as the bulk film.⁸⁴ The model is used to fit the experimentally measured ellipsometric spectra using a least squares regression with an unweighted MSE. A good quality of fit is obtained with a low MSE = 8×10^{-3} . The experimentally determined optical properties are in reasonable agreement with literature, with the index of refraction ($n = \epsilon_1^{1/2}$ when $\epsilon_2 = 0$) for electric fields oscillating parallel to the ordinary and extraordinary directions and birefringence shown in Fig. S13.^{85,88,89}

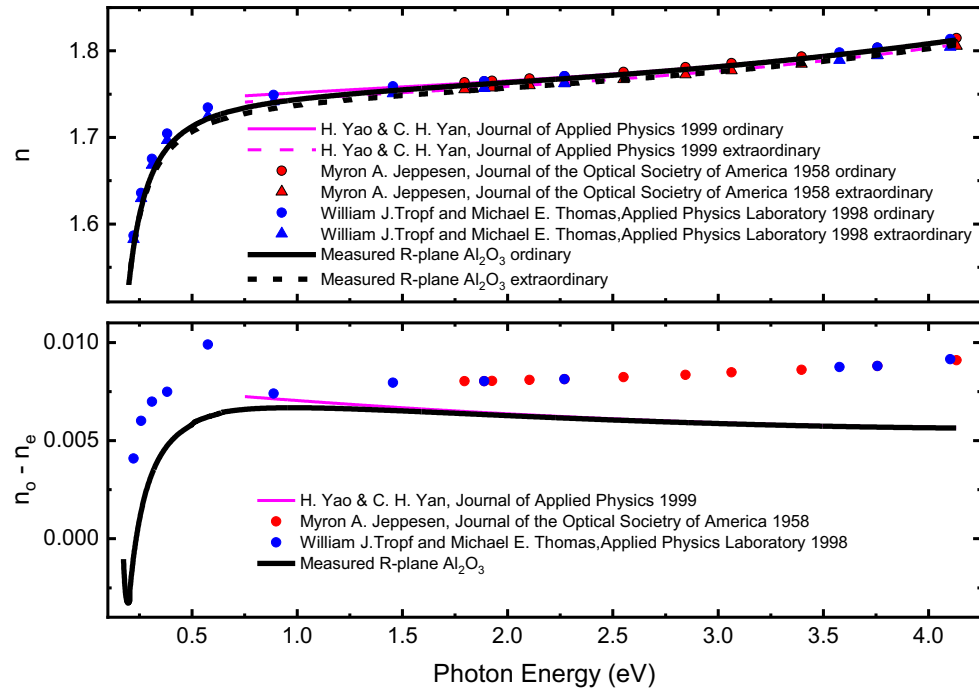


FIG. S13. Index of refraction (n) for Al₂O₃ in the ordinary (n_o) and extraordinary (n_e) direction, and birefringence ($n_o - n_e$) spectra obtained in this work compared to that reported in literature.

B. TaO₂ film

Generalized ellipsometric spectra were collected at four different sample orientations with both ellipsometers (see section II C) to determine the structural and optical properties of the TaO₂ film deposited on an *r*-plane Al₂O₃ substrates. The optical properties of Al₂O₃ were fixed from measurements of an uncoated *r*-plane Al₂O₃ substrate. TaO₂ was modeled with a rutile crystal structure with the polar Euler angle θ fixed to 33.8° , corresponding to the angle between the *c*-axis and the (101) sample surface plane.

Divided spectral range analysis^{80,90-93} was applied to determine the structural model and spectra of the dielectric function ϵ for electric fields oscillating parallel to the ordinary and extraordinary directions. Divided spectral range analysis involves simultaneously modeling the transparent spectral region and the highly absorbing spectral region of the material, each using a physically realistic parametric model to describe ϵ within that region while keeping the structural model common and excluding the weakly absorbing region. This approach avoids model-dependent bias in the weakly absorbing region near the bandgap.

The transparent region was determined to span 0.20 eV to 0.25 eV, while the highly absorbing region was selected to cover 1.15 eV to 4.13 eV. The transparent region was measured using the FTIR-VASE ellipsometer, whereas the highly absorbing region was measured using the V-VASE ellipsometer. For both the ordinary and extraordinary directions, the parametric model describing ϵ for TaO₂ in the transparent region consisted of a Sellmeier expression and a constant additive term to the real part of the complex dielectric function, ϵ_1 , denoted ϵ_∞ . In the highly absorbing region, the parametric model consisted of a Sellmeier expression, ϵ_∞ , and a series of Lorentz oscillators⁸⁶ to account for above-bandgap electronic transitions, with the number of oscillators depending on the film and crystallographic direction.

The structural model consisted of a Al₂O₃ substrate / interfacial layer / TaO₂ / air ambient stack. The interfacial layer shared the same θ as the Al₂O₃ substrate and had a fixed thickness of 1.8 nm, consistent with the surface layer established from the bare substrate measurement. The optical properties of the interfacial layer were described using an EMA^{83,84} consisting of equal fractions of Al₂O₃ and bulk TaO₂.

The TaO₂ sample had a nominal thickness of 82 nm as measured by X-ray reflectivity (XRR). Generalized spectroscopic ellipsometry fitting yielded a thicknesses of 81.7 ± 0.1 nm for the same sample, in excellent agreement with the XRR results. Deviations from the nominal angle of incidence were allowed to vary collectively and were fit to $-0.11 \pm 0.01^\circ$ for the 82 nm film in the FTIR measurements to account for differences in angle of incidence between the two ellipsometers. The azimuthal Euler angles ϕ_m were treated similarly to those of the Al₂O₃ substrate. The samples were rotated by nominal 45° increments between measurements, and each sample was placed in nominally identical orientations for each instrument.

The structural parameters and Euler angles were subsequently fixed and used as inputs for numerical inversion⁹⁴ across the entire spectral range, including the weakly absorbing region near the bandgap, to determine spectra of ϵ in both the ordinary and extraordinary directions. In the ordinary direction, a well-defined feature in ϵ_2 was observed in the 0.75 eV to 0.85 eV range, along with a broader peak spanning 2.1 eV to 2.3 eV. The absorption onset in the ordinary direction occurred in the 0.2 eV to 0.3 eV range. In the extraordinary direction, features in ϵ_2 were observed near 1.2 eV and 1.9 eV, with absorption onset occurring near 1 eV. These features are evident in the parametric and numerically inverted ϵ shown in Fig. 9 and Fig. S14, the real part of the parametric optical conductivity (σ') shown in Fig. S15, and the numerical inverted absorption coefficient (α) shown in Fig. S16.

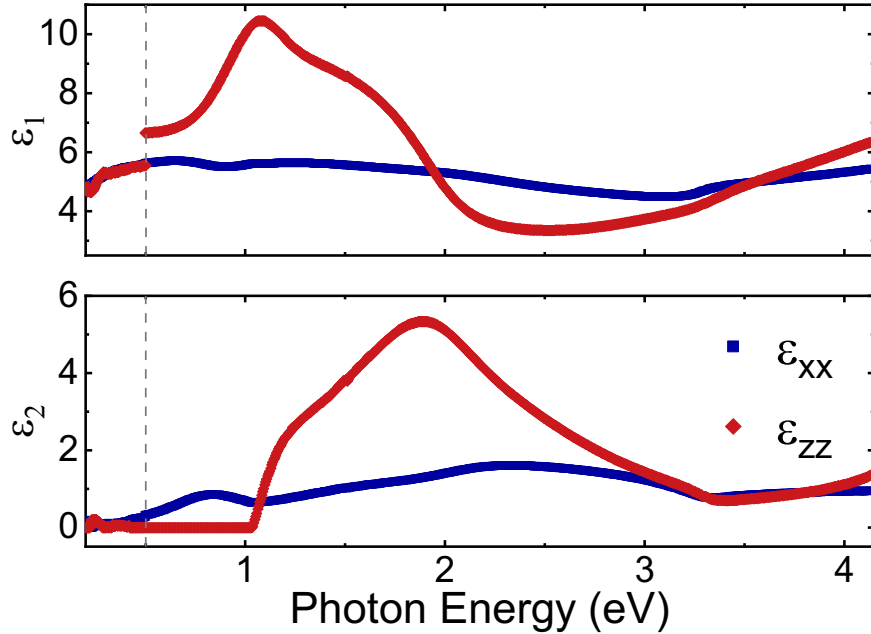


FIG. S14. Real (ϵ_1) and imaginary (ϵ_2) parts of the complex dielectric function determined by numerical inversion of spectroscopic ellipsometry measurements in the ordinary (ϵ_{xx}) and extraordinary (ϵ_{zz}) directions. The dotted line indicates the transition between two different instruments.

A series of Tauc–Lorentz oscillators⁹⁵ were fit to the measured ellipsometric spectra with the structural model fixed to values obtained from the divided spectral range analysis. The resulting ϵ spectra are shown in Fig. 9 in the main text and reproduce qualitatively similar features to the numerically inverted dielectric function while enforcing Kramers–Kronig consistency. The fitted parameters are summarized in Table S1.

The MSE values for the numerically inverted fit was 14×10^{-3} . Using the Tauc–Lorentz oscillator model yielded a nearly identical MSE value of 15×10^{-3} for the same film.

The absorption coefficient α was determined from the numerically inverted ϵ spectra for both crystallographic directions, as shown in Fig. S16. Analysis of the $(\alpha h\nu)^{1/2}$ spectra revealed two distinct slopes in the ordinary direction, indicating phonon-assisted absorption and the presence of an indirect bandgap⁹⁶. Figure S17 (a) shows linear extrapolations of $(\alpha h\nu)^{1/2} = 0$ for both slopes, with the indirect bandgap defined as the average of the intercepts. The 82 nm thick film exhibited an indirect gap of 0.32 eV. This indirect gap represents the lowest-energy optical transition and is therefore taken as the bandgap of the material. When using the Tauc–Lorentz oscillator model (Table S1), the Tauc gap parameter in the ordinary direction was fit to 0.23 eV for the 82 nm thick film. The $(\alpha h\nu)^2$ spectra were examined in both directions to identify the lowest direct transitions. Figure S18 (a) shows linear extrapolations of $(\alpha h\nu)^2 = 0$ in the ordinary direction, dominated by absorption peaks in the 0.75 eV to 0.85 eV range. The lowest direct transitions were determined to be 0.65 eV. Figure S18 (b) shows similar analysis for the extraordinary direction, yielding lowest direct transitions of 1.06 eV. Similar spectroscopic ellipsometry data were obtained for a 96 nm thick sample (not shown). The estimated uncertainty of the transition energies is on the order of 0.1 eV, arising from the choice of range for linear extrapolations.

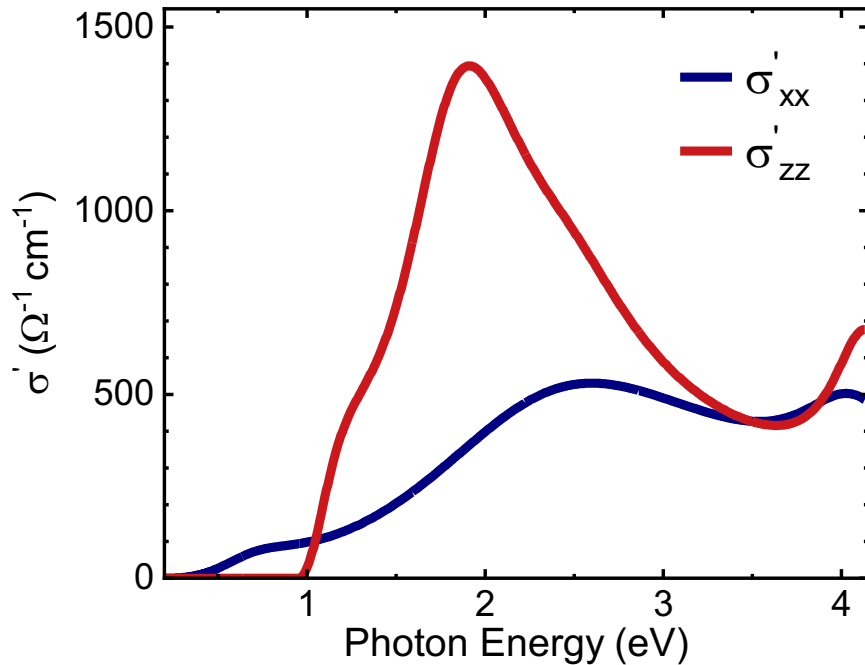


FIG. S15. Real part (σ') of the optical conductivity $\sigma = \sigma' + i\sigma''$ for an MBE-grown 82 nm thick TaO₂ film on *r*-plane sapphire in both the ordinary (σ'_{xx}) and the extraordinary (σ'_{zz}) directions. The optical conductivity was obtained from the ellipsometry data shown in Fig. 9.

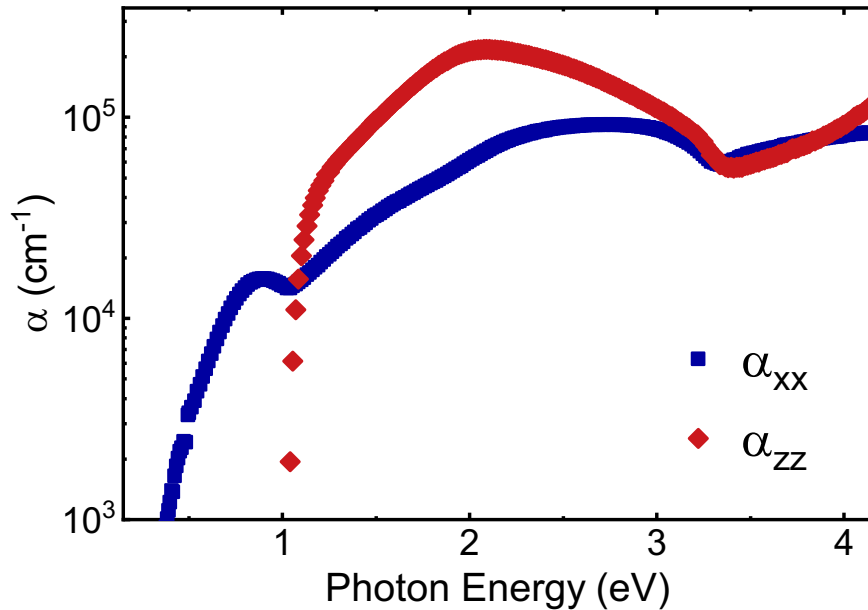


FIG. S16. Absorption coefficient α for an MBE-grown 82 nm thick TaO₂ film on *r*-plane sapphire in both the ordinary (α_{xx}) and the extraordinary (α_{zz}) directions.

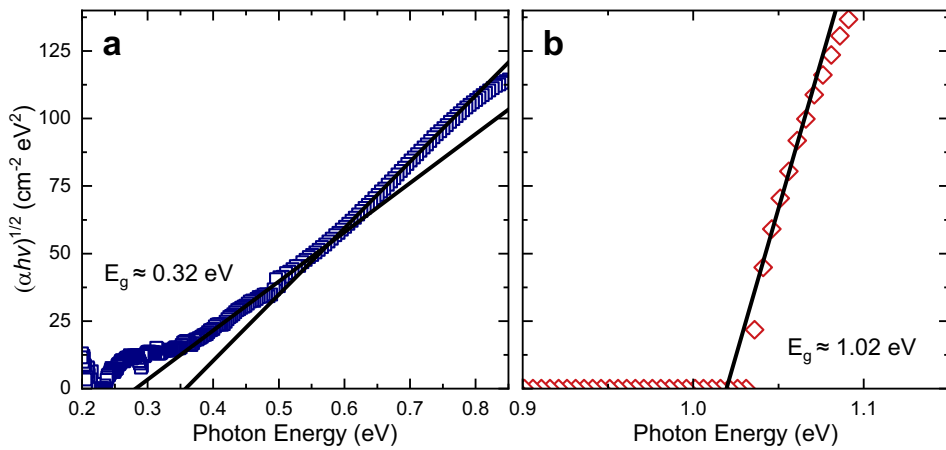


FIG. S17. Tauc plots for the extraction of the lowest indirect transition energies. The linear extrapolation of $(\alpha h\nu)^{1/2}$ to zero for the 82 nm-thick TaO₂ film in the ordinary (a) direction indicates the smallest optical transition, which is interpreted as the bandgap. There are two distinct slopes in the ordinary direction indicating phonon-assisted absorption and the presence of an indirect transition, and the intercept of both slopes are averaged to produce the bandgap energy. Panel (b) shows the same fit for the extraordinary direction, but with only a single slope indicating a lack of phonon-assisted absorption. The intercept for this fit is 1.02 eV.

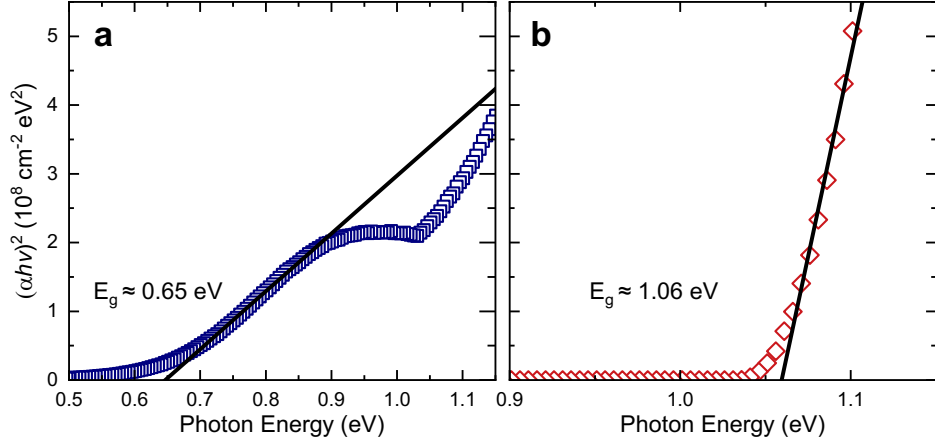


FIG. S18. Linear extrapolation of $(\alpha h\nu)^2$ to zero for the 82 nm thick TaO₂ film in the ordinary (a) and extraordinary (b) directions. The intercepts identify the lowest direct transitions.

TABLE S1. The Tauc-Lorentz amplitude (A), broadening (Γ), resonance energy (E_0) and bandgap energy (E_g) as well as the Sellmeier UV pole amplitude (A_{UV}), IR pole amplitude (A_{IR}), and the constant additive term (ϵ_∞) that describe spectra in ϵ for the TaO₂ in Fig. 9. The UV pole has a fixed energy of 6 eV and the IR pole has a fixed energy of 0 eV.

Parameter	Ordinary	Extraordinary
ϵ_∞	2.11 ± 0.03	0.78 ± 0.05
A_{UV} (eV ²)	72.5 ± 0.9	117 ± 1
A_{IR} (eV ² $\times 10^4$)	466 ± 8	1070 ± 10
E_g (eV)	0.225 ± 0.009	0.95 ± 0.01
A_1 (eV)	0.70 ± 0.06	33 ± 8
Γ_1 (eV)	0.60 ± 0.03	0.42 ± 0.03
E_{01} (eV)	0.705 ± 0.008	1.06 ± 0.03
A_2 (eV)	4.25 ± 0.07	16 ± 1
Γ_2 (eV)	2.33 ± 0.04	0.85 ± 0.04
E_{02} (eV)	2.53 ± 0.01	1.812 ± 0.007
A_3 (eV)	0.37 ± 0.04	1.1 ± 0.3
Γ_3 (eV)	0.761 ± 0.06	0.84 ± 0.09
E_{03} (eV)	4.07 ± 0.02	2.50 ± 0.03
A_4 (eV)	—	0.58 ± 0.05
Γ_4 (eV)	—	0.47 ± 0.03
E_{04} (eV)	—	4.14 ± 0.02

S12. FIRST-PRINCIPLES CALCULATIONS

A. Computational Details

In order to investigate the properties of TaO₂, first-principles density functional theory calculations were performed using VASP 6.2.0,^{97–99} using the projector augmented-wave (PAW) method. We explored the properties with the following exchange-correlation functionals: local-density approximation (LDA), Perdew-Burke-Ernzerhof (PBE), and PBEsol,¹⁰⁰ and found that the general features of TaO₂ were consistent regardless of the choice of functional (Sec. S12 C). In contrast to experimental conditions, our calculations assume an infinite periodic crystal with zero epitaxial strain. Our calculations show that the (rutile-like) *P*4₂/*mnm* high symmetry structure is metallic and that there exists a lower energy, lower symmetry *I*4₁/*a* structure, which is insulating. The band gap in the *I*4₁/*a* phase is sensitive to the value of the Hubbard *U*, see Sec. S12 B. Our results are similar to the findings of Ref.¹⁰¹, however these previous authors claim the lower symmetry structure has space group *P*1 as opposed to our identification of *I*4₁/*a*.

The following states were included in the valence of the PAW potentials: 5*p*⁶5*d*⁴6*s*¹ for tantalum and 2*s*²2*p*⁴ for oxygen. A force convergence tolerance of 5×10^{-4} eV/Å was used for all calculations with a plane-wave energy cutoff of 900 eV. A 16×16×27 Monkhorst-Pack **k**-point grid was used for calculations of the *P*4₂/*mnm* structure using the conventional 6-atom unit cell and an 11×11×11 **k**-point grid was used for the *I*4₁/*a* structure in the primitive 24-atom unit cell. These values were chosen to converge the lattice constants of the *P*4₂/*mnm* phase (which requires more stringent parameters as it is metallic) to within 0.5 picometers when compared to incrementing the **k**-point grid to 20×20×40 and the energy cutoff to 1900 eV. Gaussian smearing was used in our calculations on the *P*4₂/*mnm* phase, with a smearing width of 0.09 eV such that the entropy term was between 1 and 2 meV/atom (LDA 1.08 meV/atom, PBE 1.14 meV/atom, PBEsol 1.08 meV/atom). Calculations on the *I*4₁/*a* phase were also performed with Gaussian smearing.

We found that the occupation of the tantalum-*d* orbital was sensitive to the application of an on-site Coulomb interaction (Hubbard *U*) using LDA+U/GGA+U as implemented by Dudarev.¹⁰² The values of the on-site term (*U* – *J*) for each of the exchange correlation-functionals were found using the linear response approach defined in Ref.¹⁰³. The *U* – *J* values extracted from this method for the low-symmetry structures (LDA 4.13 eV, PBE 3.95 eV, and PBEsol 3.97 eV) were used for calculations involving the high-symmetry *P*4₂/*mnm* structure as they did not differ significantly from the self-consistent *U* – *J* values calculated in the high-symmetry structure (LDA: 4.22 eV, PBE 4.17 eV, and PBEsol 3.97 eV). Our converged lattice constants using these *U* values can be found in Table S3. It should be noted that while the on-site occupation had a linear response to the on-site value for small *U* – *J*, a second order term becomes appreciable as the *U* – *J* term approaches 4 eV (Fig. S19), which is concerning when assuming a linear response. We explore the sensitivity of properties due to the applied Hubbard *U* in further detail in Sec. S12 B.

We used a **k**-point grid of 32×32×54 for the *P*4₂/*mnm* phase and 19×19×19 for the *I*4₁/*a* phase when calculating the density of states. The frequency-dependent dielectric response was calculated using the built-in LOPTIC method in VASP¹⁰⁴. The current-based results are reported for the *P*4₂/*mnm* phase as it is metallic and the direct-based results are reported for the *I*4₁/*a* phase, as recommended by Ref.¹⁰⁵. For all of the density of states, electronic band structure, and frequency-dependent dielectric response calculations the number of electronic bands which were included were 84 for the *P*4₂/*mnm* phase and 336 for the *I*4₁/*a* phase. Below are our fully relaxed structures (*P*4₂/*mnm* and *I*4₁/*a*) for the LDA functional with a Hubbard *U* value of 4.127 eV.

```
TaO2 - P4_2/mnm
1.000000000000000
4.9793858837262732 0.000000000000000 0.000000000000000
0.000000000000000 4.9793858837262732 0.000000000000000
0.000000000000000 0.000000000000000 2.8575942530325609

Ta 0
2 4
Direct
-0.000000000000000 -0.000000000000000 -0.000000000000000
0.500000000000000 0.500000000000000 0.500000000000000
0.2847778905047560 0.2847778905047560 0.000000000000000
0.7152221094952438 0.7152221094952438 -0.000000000000000
0.2152221094952439 0.7847778905047562 0.500000000000000
0.7847778905047562 0.2152221094952439 0.500000000000000
```

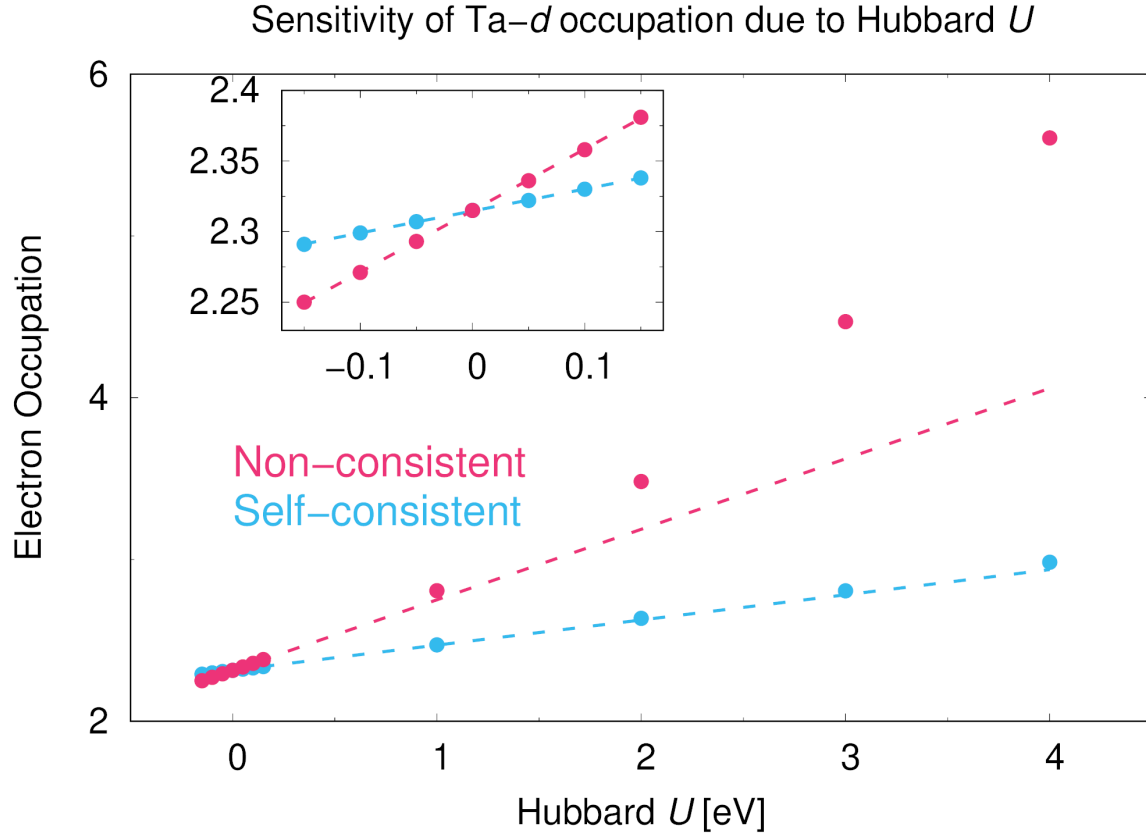


FIG. S19. Dependence of the Ta-*d* occupation as a function of the Hubbard U for the $I4_1/a$ structure using the LDA functional. The red data points correspond to the non-consistent results, whereas the blue data points correspond to the self-consistent results. The inset shows the data points close to zero which were used to fit the linear slopes to calculate the self-consistent value of U (4.127 eV). We note that a second order term becomes comparable to the linear term for the non-consistent results as U approaches 4 eV.

TaO2 - I4_1/a

1.000000000000000		
-4.8757749036197104	4.8757749050696697	2.9700177379407555
4.8757749036197104	-4.8757749050696697	2.9700177379407555
4.8757749050696697	4.8757749036197104	-2.9700177379407555

Ta 0

8 16

Direct

0.6408907722002998	0.8879626861270091	0.7339791835272080
0.1091092277997002	0.3620373138729907	0.7660208164727920
0.1539835025998012	0.9069115886730916	0.2660208164727919
0.5960164974001989	0.3430884113269082	0.2339791835272080
0.0930884113269082	0.3591092277997002	0.2470719139267094
0.6569115886730916	0.8908907722002998	0.2529280860732906
0.6379626861270091	0.4039835025998012	0.7470719139267094
0.1120373138729908	0.8460164974001989	0.7529280860732906
0.7547370189934782	0.0015142385332747	0.0249475590730972
0.2796315625974120	0.5317837384311869	0.0527699818039243
0.2709862433727373	0.0231384193065140	0.5527699818039243
0.7734333205398225	0.5202105399796104	0.5249475590730970
0.9952629810065147	0.2484857614667254	0.4750524409269028
0.4703684374025880	0.7182162615688131	0.4472300181960757
0.4790137566272627	0.2268615806934860	0.9472300181960757
0.9765666794601775	0.7297894600203896	0.9750524409269030
0.2702105399796103	0.2452629810065148	0.2467772195397895
0.7731384193065139	0.7203684374025879	0.2521521759337697
0.7515142385332748	0.2265666794601776	0.7467772195397895
0.2817837384311871	0.7290137566272626	0.7521521759337695
0.9768615806934861	0.5296315625974121	0.2478478240662305
0.4797894600203897	0.0047370189934852	0.2532227804602105
0.4682162615688129	0.5209862433727374	0.7478478240662305
0.9984857614667252	0.0234333205398225	0.7532227804602105

B. Ta-*d* Hubbard *U* Sensitivity

Our calculations suggest that the properties of the $I4_1/a$ phase of TaO₂ are sensitive to the value of the Hubbard *U* parameter for the Ta-*d* states. In this section we show how the properties compare with the LDA exchange correlation functional for *U* values of 0 eV, 2 eV, and 4.127 eV. The structural instability observed in Fig. S20 corresponds to displacements of the R_1^+ mode of $P4_2/mnm$, which in turn brings Γ_1^+ , Γ_3^+ and M_5^+ displacements into the fully relaxed structure via higher-order coupling terms. There are a number of possible high-symmetry configurations of the 4-dimensional R_1^+ distortion. We found that the [a,a,-a,a] configuration (which takes the $P4_2/mnm$ structure to $I4_1/a$) had the lowest total energy compared to the other possible combinations. Most configurations raised the total energy compared to $P4_2/mnm$, the different configurations can be found using the ISOSUBGROUP tool.^{106,107} A peculiar feature of the transition from $P4_2/mnm$ to $I4_1/a$ is that the energy landscape has a barrier which depends on the Hubbard *U* (Fig. S20). There is a finite barrier for *U* = 0 eV which must be overcome before the system lowers in energy, this could potentially be why this lower-energy phase was missed in prior explorations¹⁰⁸. Increasing *U* to 2 eV lowers the barrier, but it is still non-zero. When *U* is set to 4.127 eV the barrier is gone and the transition is purely downhill. The structure also changes volume as the $P4_2/mnm$ structure relaxes to $I4_1/a$. Fig. S20b shows that there still is an energy barrier even as the volume changes for the *U* = 0 eV and 2 eV cases, and again is absent in the *U* = 4.127 eV case. Applying the volume deformations without the associated atomic displacements only increased the total energy. The lattice constants of the fully relaxed cells for these different *U* values can be found in Table S2. The *a* and *c*-axes grow as *U* increases in the $P4_2/mnm$ structure, and only the *a*-axis grows in the $I4_1/a$ structure while the *c*-axis appears to be relatively insensitive to *U*.

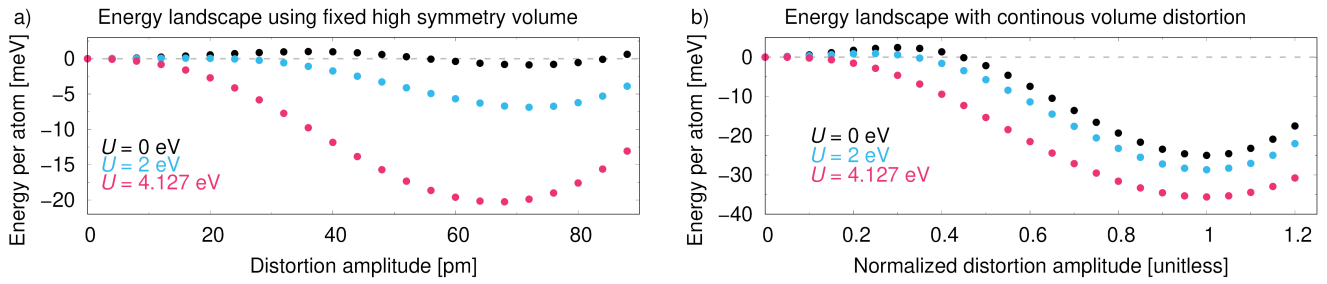


FIG. S20. Energy landscapes from our first-principle calculations from the high-symmetry $P4_2/mnm$ structure to the low-symmetry $I4_1/a$ structure. a) The continuous distortion of atoms from the $P4_2/mnm$ structure to the relaxed $I4_1/a$, with a fixed $P4_2/mnm$ volume. Each value of *U* had its own relaxed $P4_2/mnm$ and $I4_1/a$ structures, and the distortions were defined as the difference in atomic positions between the two. b) Continuous distortion of atoms along with a continuous strain deformation associated with the transition between $P4_2/mnm$ (at 0) and $I4_1/a$ (at 1), for the three different *U* values. The computational cell for both of these panels was a 48 atom $2 \times 2 \times 2$ supercell of the 6 atom conventional cell, and an $8 \times 8 \times 14$ \mathbf{k} -point grid was used.

TABLE S2. Lattice constants after volume relaxation with the LDA exchange-correlation functional, for the different values of *U*. The $I4_1/a$ lattice constants have been converted to reference the 6-atom conventional cell.

Hubbard <i>U</i> [eV]	0	2	4.127
$P4_2/mnm$ <i>a</i> -axis [\AA]	4.919	4.947	4.979
$P4_2/mnm$ <i>c</i> -axis [\AA]	2.843	2.850	2.858
$I4_1/a$ <i>a</i> -axis [\AA]	4.774	4.816	4.876
$I4_1/a$ <i>c</i> -axis [\AA]	2.977	2.978	2.970

In addition to the existence of an energy barrier between the $P4_2/mnm$ and $I4_1/a$ phases, the electronic properties of the $I4_1/a$ phase of TaO₂ are also sensitive to the value of *U*. The density of states in Fig. S21 show that while the $P4_2/mnm$ phase is relatively insensitive to the Hubbard *U* value the $I4_1/a$ phase becomes an insulator as the Hubbard *U* value is increased from zero, with the gap increasing for larger values of *U*. Applying the Hubbard *U* on the Ta-*d* states is pushing them away from the Fermi energy in the $I4_1/a$ phase. The electronic band structure calculations in Fig. S22 also show electronic states at the Fermi energy separate as the value of *U* increases in the $I4_1/a$ phase.

Figures S23 and S24 show how *U* alters the frequency-dependent dielectric response in the $P4_2/mnm$ and $I4_1/a$ phases respectively. The low-frequency imaginary component in the $P4_2/mnm$ phase goes to infinity because it is a metal, and the position of the resonant absorption peaks do not change much as a function of *U*. The $I4_1/a$ phase on the other-hand exhibits significant changes to the absorption spectrum with *U*, particularly along the *z*-axis. As we have demonstrated repeatedly

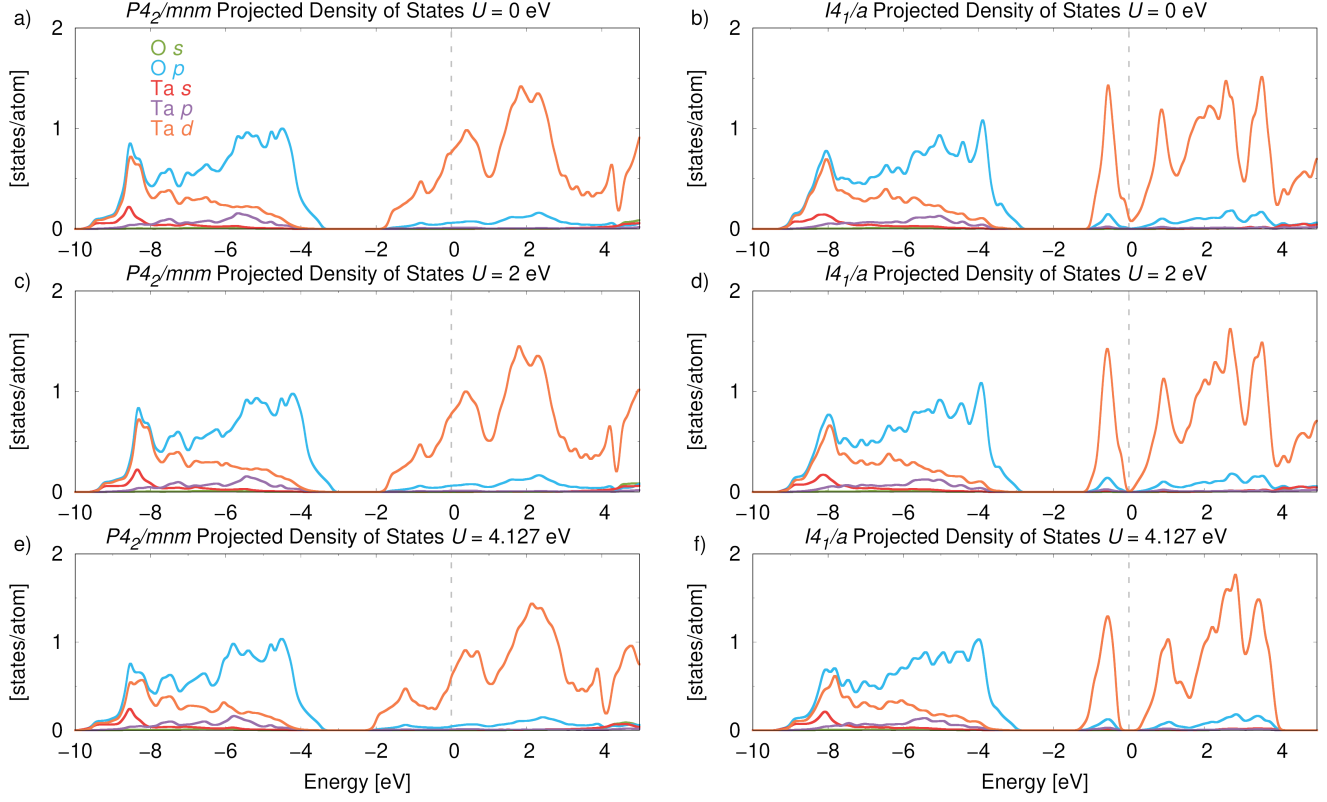


FIG. S21. First-principle calculation of the density of states in the $P4_2/mnm$ (panels a, c, e) and $I4_1/a$ (panels b, d, f) phases with the LDA functional for various Hubbard U values. The $P4_2/mnm$ phase appears relatively insensitive to the Hubbard U , and most of the electronic states at the Fermi energy are from Ta- d . The $I4_1/a$ phase goes from having no gap at $U = 0$ eV, to having a band gap which grows as U increases.

throughout this section, the $I4_1/a$ phase of TaO₂ is quite sensitive to the value of the Hubbard U and warrants further exploration.

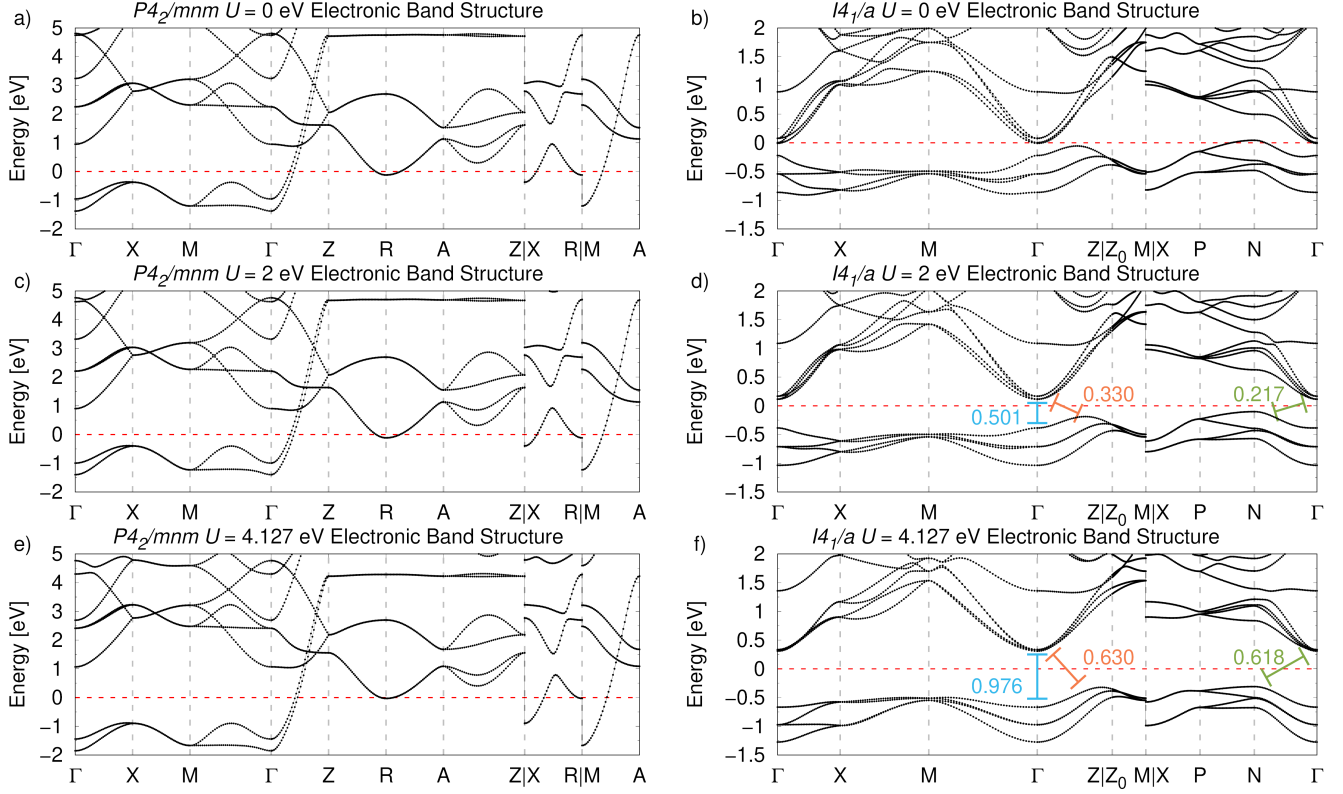


FIG. S22. First-principles electronic band structures for the $P4_2/mnm$ (panels a, c, and e) and $I4_1/a$ phases (panels b, d, and f) for different values of the Hubbard U . The $P4_2/mnm$ phase seems relatively insensitive to the Hubbard U , and has states at the Fermi energy indicating that the high-symmetry phase is metallic. The $I4_1/a$ phase starts with states at the Fermi energy for $U = 0$ eV, but a gap forms as the Hubbard U increases.

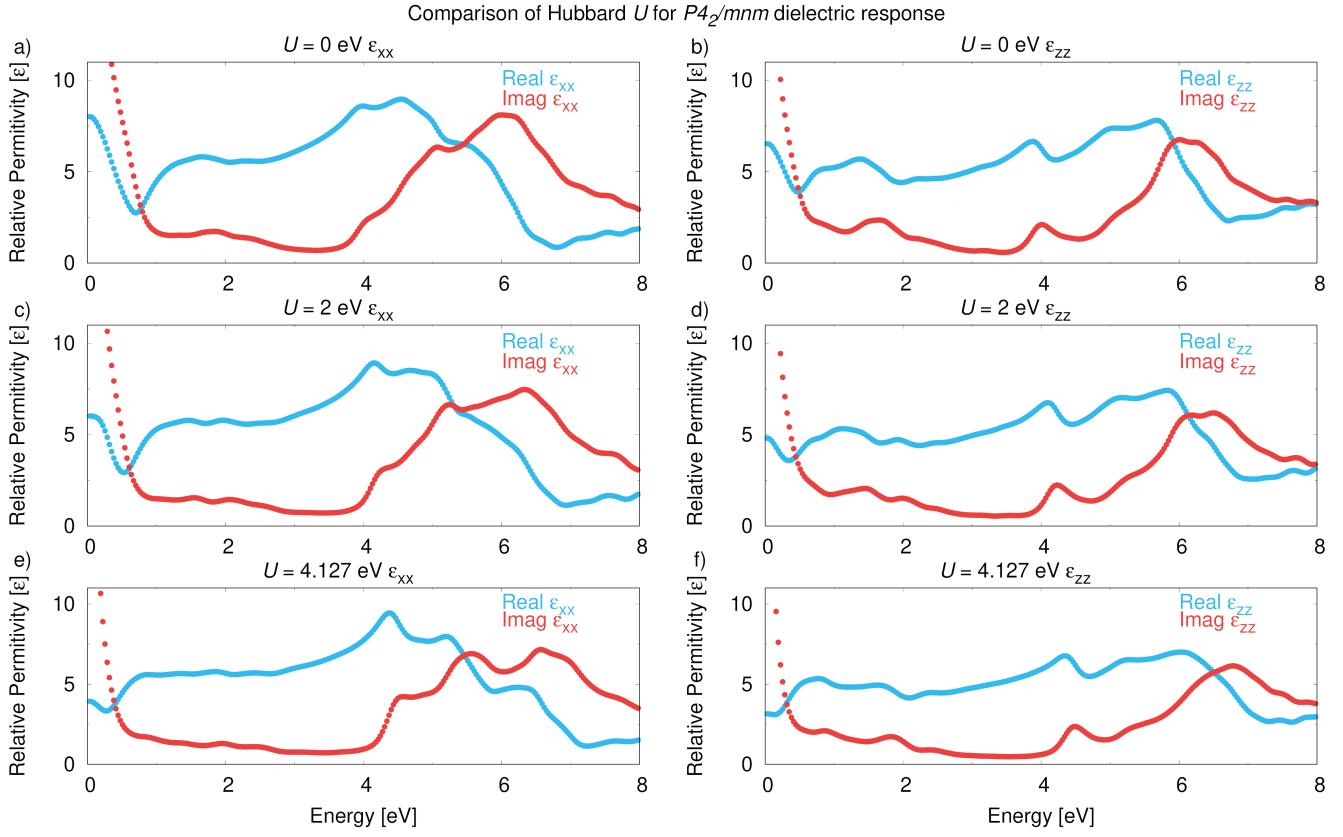


FIG. S23. First-principle results of the frequency-dependent relative permittivity in the $P4_2/mnm$ phase for the LDA functional. The left column of panels (a, c, and e) show the real and imaginary components along the x -direction (symmetry equivalent to y), while the right column of panels (b, d, and f) shows the real and imaginary components along the z -axis.

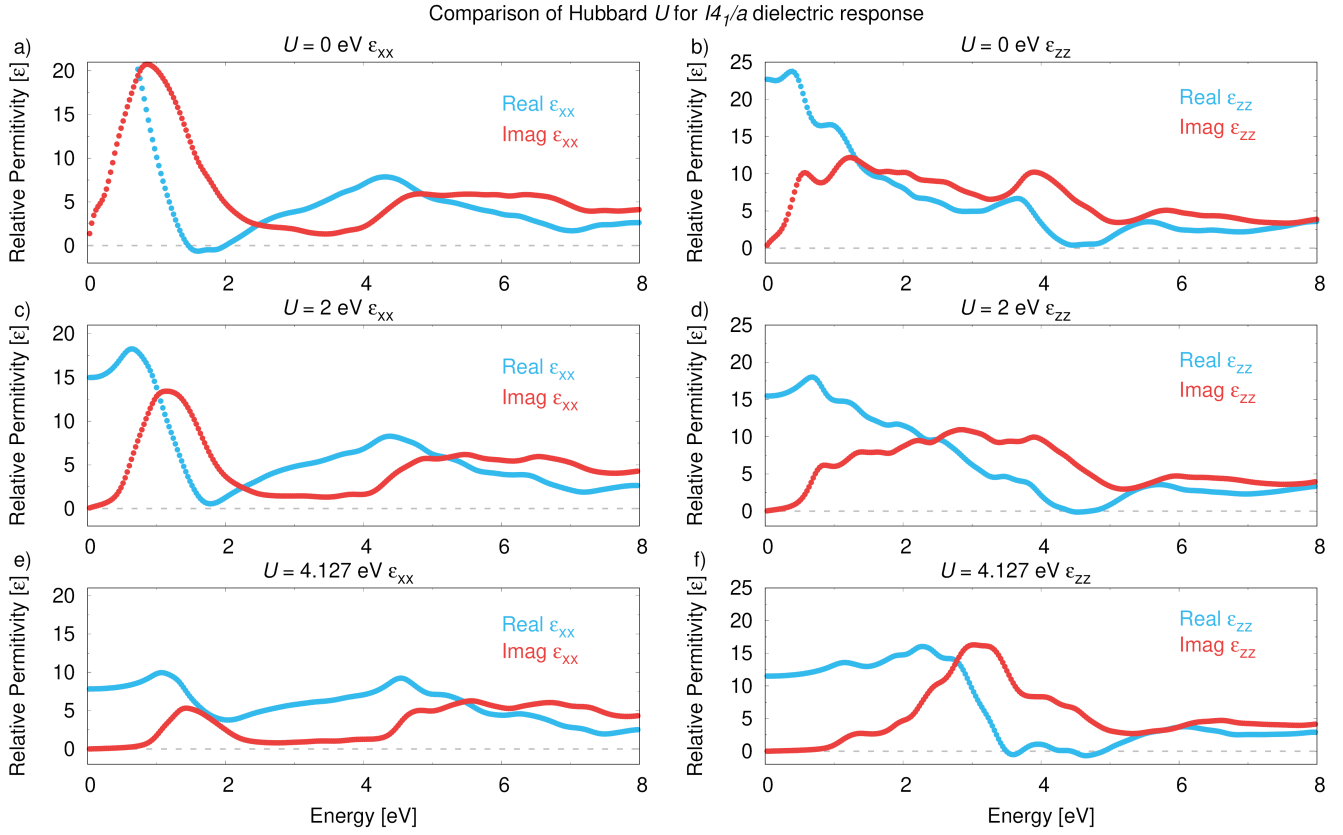


FIG. S24. First-principle results of the frequency-dependent relative permittivity in the $I4_1/a$ phase for the LDA functional. The left column of panels (a, c, and e) show the real and imaginary components along the x -direction (symmetry equivalent to y), while the right column of panels (b, d, and f) shows the real and imaginary components along the z -axis.

C. Comparing Functionals

The general features from our first-principles calculations of TaO₂ seem consistent for the variety of exchange-correlation functionals that we checked. The lattice constants in Table S3 are the shortest in LDA, the longest in PBE, and in-between for PBEsol, which is the expected trend since LDA has a tendency to ‘over-bond.’ All three functionals feature an elongation of the *c*-axis and a contraction of the *a/b*-axes as the system transitions from the *P4₂/mnm* phase to the *I4₁/a* phase.

The projected density of states of the *P4₂/mnm* and *I4₁/a* phases are visually consistent between the different functionals (Fig. S25). The *P4₂/mnm* phase has Ta-*d* states at the Fermi energy, indicating the system is metallic. This is in contrast to the *I4₁/a* phase, which has a band gap at the Fermi energy. The band structure calculations (Fig. S26) suggest the gap is smallest for an indirect transition, while the smallest direct gap is roughly 1 eV. The frequency-dependent dielectric response (Figs. S27 and S28) have fairly consistent spectra across the different functionals.

TABLE S3. First-principles relaxed lattice constants, for the various exchange-correlation functionals. The *I4₁/a* lattice constants have been converted to match the 6-atom conventional cell.

Functional	LDA	PBE	PBEsol
Ta- <i>d</i> Hubbard <i>U</i> [eV]	4.127	3.955	3.966
<i>P4₂/mnm</i> <i>a</i> -axis [Å]	4.979	5.054	5.012
<i>P4₂/mnm</i> <i>c</i> -axis [Å]	2.858	2.902	2.872
<i>I4₁/a</i> <i>a</i> -axis [Å]	4.876	4.971	4.915
<i>I4₁/a</i> <i>c</i> -axis [Å]	2.970	3.000	2.981

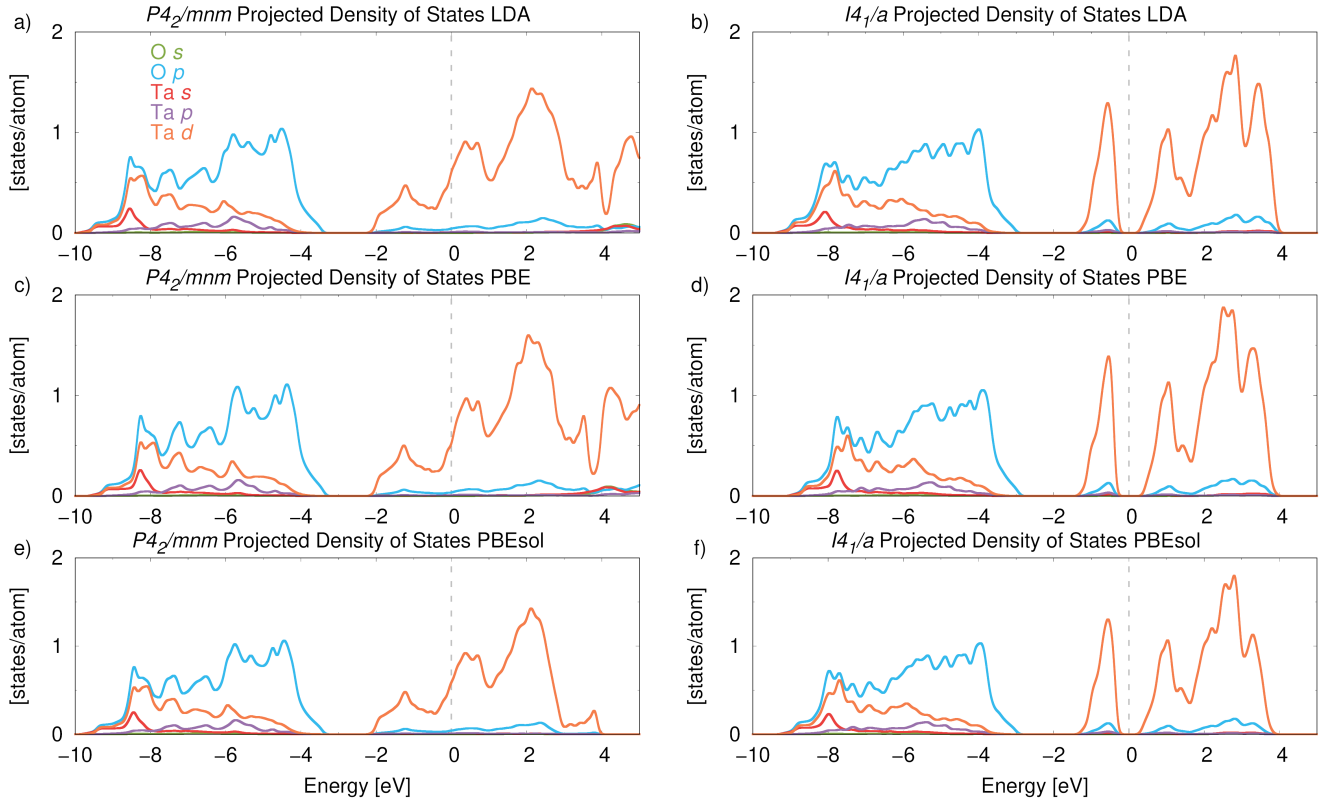


FIG. S25. First-principle calculation of the density of states of the *P4₂/mnm* (panels: a, c, and e) and *I4₁/a* (panels: b, d, f) phases for each of the LDA (a & b), PBE (c & d), and PBEsol (e & f) functionals. The respective Hubbard *U* for each functional is: 4.127 eV for LDA, 3.955 eV for PBE, and 3.966 eV for PBEsol.

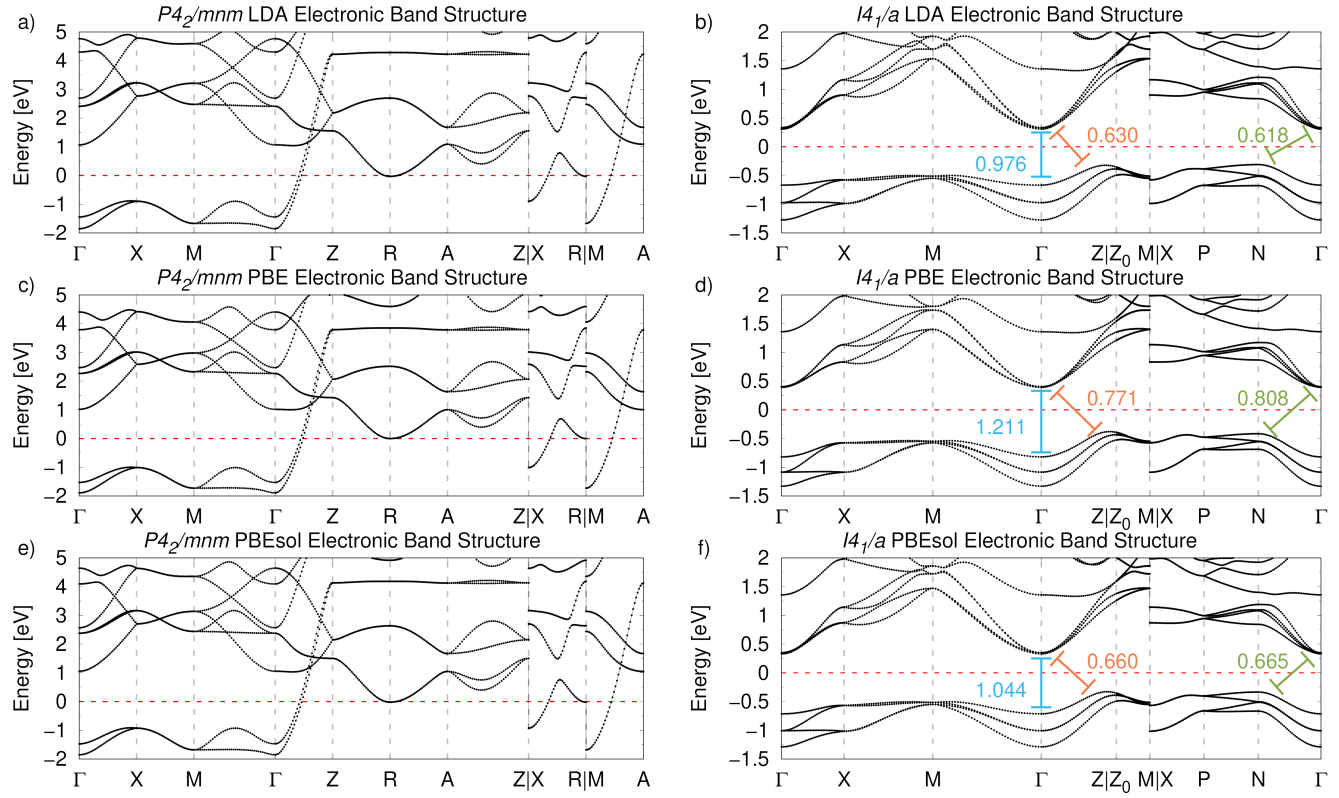


FIG. S26. First-principles electronic band structures for each functional for the $P4_2/mnm$ (panels a, c, and e) and $I4_1/a$ phases (panels b, d, and f). In the $P4_2/mnm$ phase, each functional has electronic states at the Fermi energy, indicating that the high symmetry phase is metallic. In the $I4_1/a$ phase, each functional has a direct band gap of ~ 1 eV and an indirect gap of ~ 0.7 eV. The respective Hubbard U for each function is: 4.127 eV for LDA, 3.955 eV for PBE, and 3.966 eV for PBEsol.

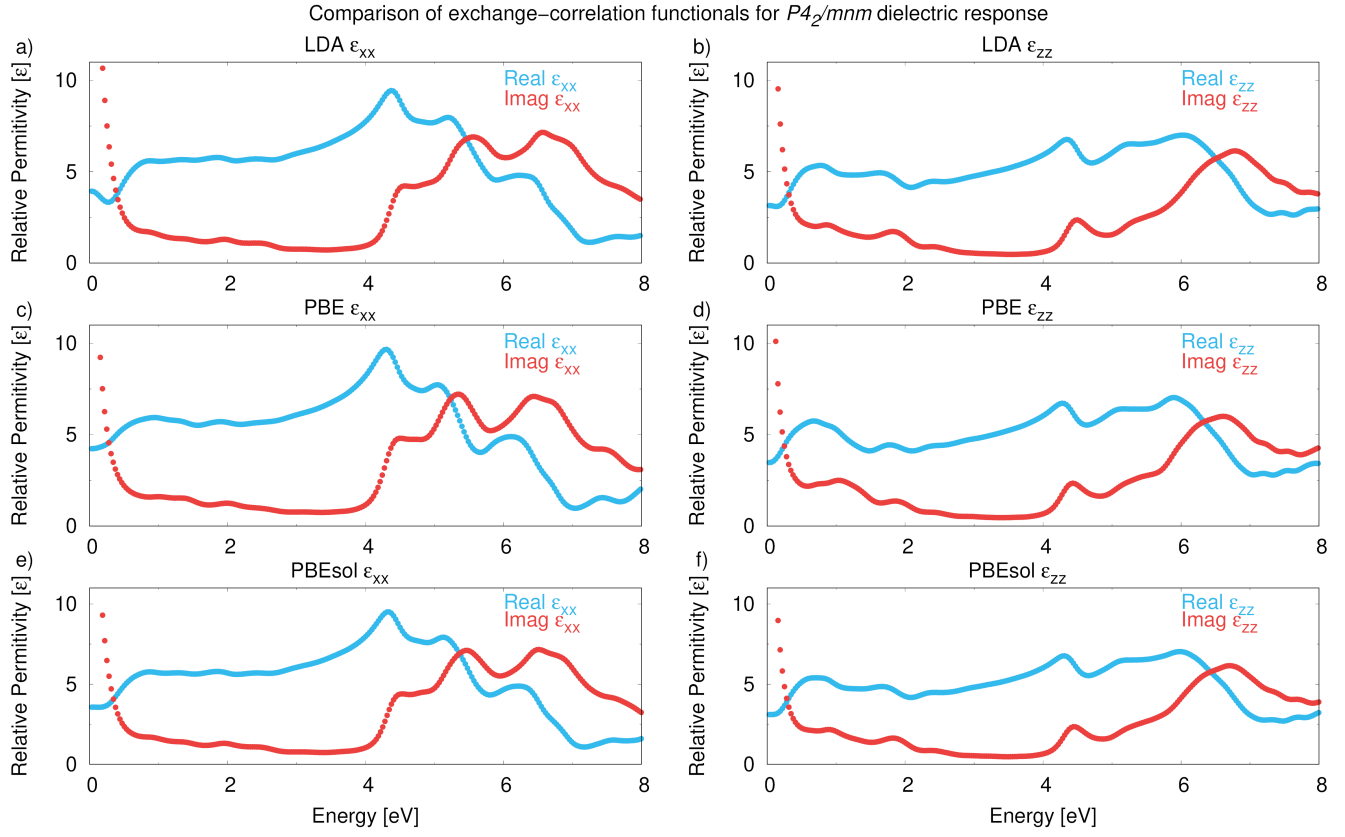


FIG. S27. First-principle results of the frequency dependent relative permittivity in the $P4_2/mnm$ phase for the LDA (a, b), PBE (c, d), and PBEsol (e, f) functionals. The left column of panels (a, c, and e) show the real and imaginary components along the x -direction (symmetry equivalent to y), while the right column of panels (b, d, and f) show the real and imaginary components along the z -axis. The imaginary component goes to infinity at low frequency because the phase is a metal. The respective Hubbard U for each function is: 4.127 eV for LDA, 3.955 eV for PBE, and 3.966 eV for PBEsol.

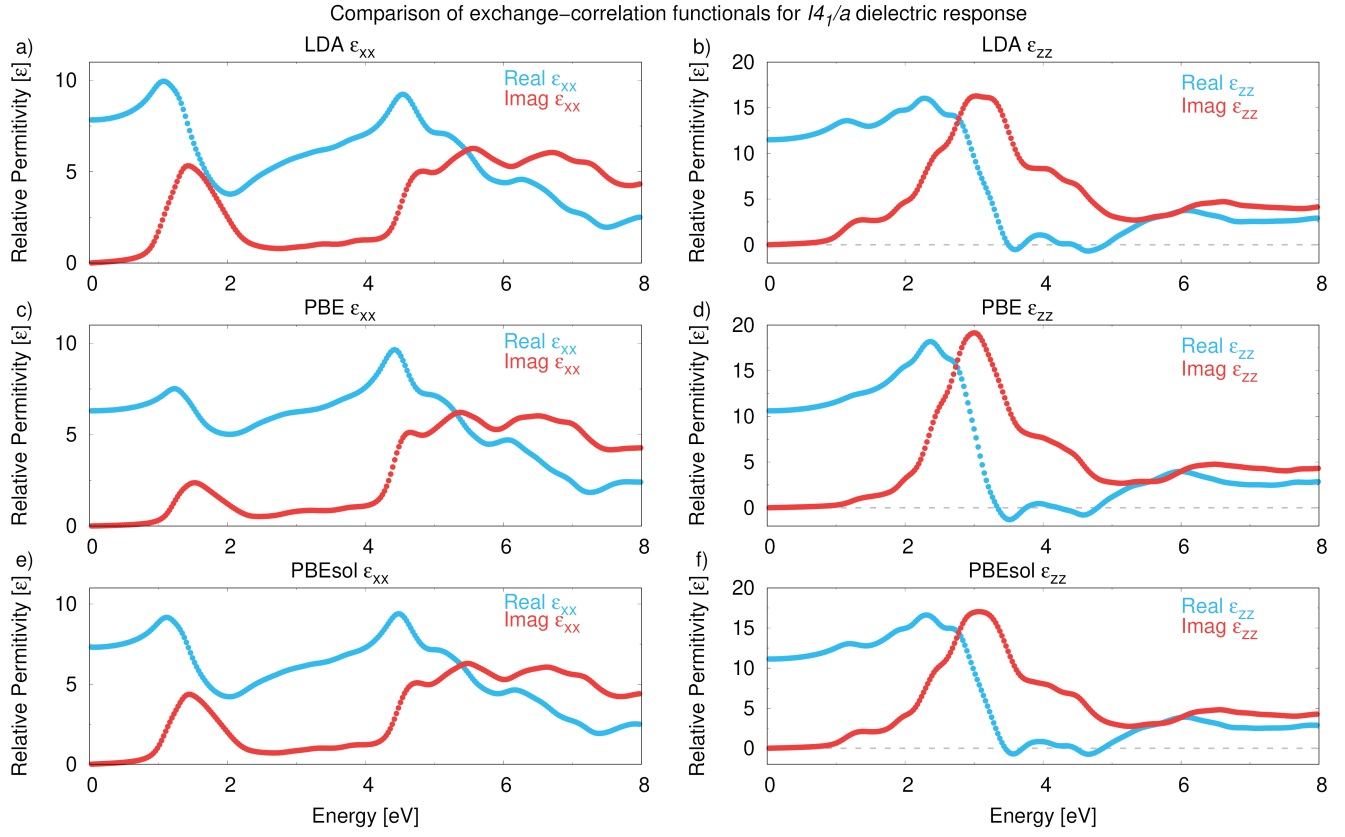


FIG. S28. First-principle results of the frequency dependent relative permittivity in the $I4_1/a$ phase for the LDA (a, b), PBE (c, d), and PBEsol (e, f) functionals. The left column of panels (a, c, and e) show the real and imaginary components along the x -direction (symmetry equivalent to y), while the right column of panels (b, d, and f) show the real and imaginary components along the z -axis. The respective Hubbard U for each function is: 4.127 eV for LDA, 3.955 eV for PBE, and 3.966 eV for PBEsol.